Monthly Notices of the ROYAL ASTRONOMICAL SOCIETY

MNRAS **435,** 1108–1125 (2013) doi:10.1093/mnras/stt1345
Advance Access publication 2013 August 28

A multiwavelength view of cooling versus AGN heating in the X-ray luminous cool-core of Abell 3581★

R. E. A. Canning,[1,2]† M. Sun,[3] J. S. Sanders,[4] T. E. Clarke,[5] A. C. Fabian,[6] S. Giacintucci,[7,8] D. V. Lal,[9] N. Werner,[1,2] S. W. Allen,[1,2,10] M. Donahue,[11] A. C. Edge,[12] R. M. Johnstone,[6] P. E. J. Nulsen,[13] P. Salomé[14] and C. L. Sarazin[15]

[1]*Kavli Institute for Particle Astrophysics and Cosmology (KIPAC), Stanford University, 452 Lomita Mall, Stanford, CA 94305-4085, USA*
[2]*Department of Physics, Stanford University, 452 Lomita Mall, Stanford, CA 94305-4085, USA*
[3]*Eureka Scientific Inc., 2452 Delmer Street Suite 100, Oakland, CA 94602-3017, USA*
[4]*Max-Planck-Institut für extraterrestrische Physik (MPE), Giessenbachstrasse, D-85748 Garching, Germany*
[5]*Naval Research Laboratory, 4555 Overlook Avenue SW, Code 7213, Washington, DC 20375, USA*
[6]*Institute of Astronomy, Madingley Road, Cambridge CB3 0HA, UK*
[7]*Department of Astronomy, University of Maryland, College Park, MD 20742-2421, USA*
[8]*Joint Space-Science Institute, University of Maryland, College Park, MD 20742-2421, USA*
[9]*National Centre for Radio Astrophysics (NCRA-TIFR), Pune University Campus, Ganeshkhind PO Pune 411 007, India*
[10]*SLAC National Accelerator Laboratory, 2575 Sand Hill Road, Menlo Park, CA 94025, USA*
[11]*Michigan State University, 567 Wilson Rd. Rm 3275, East Lansing, MI 48824, USA*
[12]*Institute of Computational Cosmology, University of Durham, Durham DH1 3LE, UK*
[13]*Harvard–Smithsonian Center for Astrophysics, 60 Garden Street, Cambridge, MA 02138, USA*
[14]*LERMA & UMR8112 du CNRS, Observatoire de Paris, 61 Av. de l'Observatoire, F-75014 Raris, France*
[15]*Department of Astronomy, University of Virginia, 530 McCormick Road, Charlottesville, VA 22904, USA*

Accepted 2013 July 18. Received 2013 July 17; in original form 2013 April 27

ABSTRACT

We report the results of a multiwavelength study of the nearby galaxy group, Abell 3581 ($z = 0.0218$). This system hosts the most luminous cool core of any nearby group and exhibits active radio mode feedback from the supermassive black hole in its brightest group galaxy, IC 4374. The brightest galaxy has suffered multiple active galactic nucleus outbursts, blowing bubbles into the surrounding hot gas, which have resulted in the uplift of cool ionized gas into the surrounding hot intragroup medium. High velocities, indicative of an outflow, are observed close to the nucleus and coincident with the radio jet. Thin dusty filaments accompany the uplifted, ionized gas. No extended star formation is observed; however, a young cluster is detected just north of the nucleus. The direction of rise of the bubbles has changed between outbursts. This directional change is likely due to sloshing motions of the intragroup medium. These sloshing motions also appear to be actively stripping the X-ray cool core, as indicated by a spiralling cold front of high-metallicity, low-temperature, low entropy gas.

Key words: galaxies: active – galaxies: clusters: intracluster medium – Galaxies: groups: individual: Abell 3581 – galaxies: ISM.

1 INTRODUCTION

The last decade has seen significant progress into the cooling flow phenomenon in 'cool-core' clusters of galaxies. These clusters are so named as they exhibit sharply peaked X-ray surface brightness profiles resulting from their cool, high-density X-ray cores. The cooling time of the gas in these cores is significantly shorter than the Hubble time.

If no sources of heat are present, the observed high central X-ray luminosities would imply mass cooling rates as high as hundreds or thousands of solar masses a year (e.g. Fabian 1994 and references therein). However, with the advent of the *XMM–Newton* space telescope, high-resolution spectra exposed a lack of strong X-ray emission below 1 keV in cool-core clusters. The implication of these observations was a reduction in the inferred net X-ray cooling rates and an effective quenching of any resulting star formation (for reviews see Peterson & Fabian 2006 and McNamara & Nulsen

★ Based on observations obtained at the Southern Astrophysical Research (SOAR) telescope, which is a joint project of the Ministério da Ciência, Tecnologia, e Inovação (MCTI) da República Federativa do Brasil, the US National Optical Astronomy Observatory (NOAO), the University of North Carolina at Chapel Hill (UNC) and Michigan State University (MSU).
† E-mail: rcanning@stanford.edu

2007). The most probable source of heating to quench the cooling of the intracluster medium (ICM) is provided by outbursts from the supermassive black hole (SMBH) lurking at the centre of the central, dominant, brightest cluster galaxies (BCGs) (for a review of the observational evidence for BH feedback see Fabian 2012).

The prevalence of Hα emission in BCGs has long been known (e.g. Lynds 1970; Cowie et al. 1983; Hu et al. 1983; Johnstone, Fabian & Nulsen 1987; Heckman et al. 1989; Crawford et al. 1999; Donahue et al. 2000; Fabian et al. 2001; Conselice, Gallagher & Wyse 2001) and has been shown to have diverse and dramatic morphologies. These ionized gas nebulosities surround about a third of all BCGs but are found preferentially in cool-core clusters. The luminosity of the Hα bright nebulosities ranges from 10^{39} to 10^{43} erg s^{-1} and can extend over 70 kpc from the core of the BCG (Crawford & Fabian 1992; Crawford et al. 1999). The emission is well correlated with both the X-ray luminosity and with emission lines from molecular gas. Developments in optical astronomy, particularly with the progression of integral field spectroscopy (IFS), have allowed the spatio-kinematic properties of the gaseous nebulae surrounding BCGs to be better probed. For example, the spatial, kinematical and excitation properties of the ionized and molecular gas has now been mapped in small samples of BCGs (e.g. Wilman, Edge & Swinbank 2006; Hatch, Crawford & Fabian 2007; Edwards et al. 2009; Wilman, Edge & Swinbank 2009; Farage et al. 2010; Oonk et al. 2010; Canning et al. 2011; Farage, McGregor & Dopita 2012).

In addition to ionized gas nebulosities, many cool-core BCGs contain significant masses of cold molecular gas and dust, both in the centres of the galaxies and farther out. This is often coincident with the extended ionized gas filaments in the galaxy outskirts (e.g. Jaffe & Bremer 1997; Donahue et al. 2000; Edge 2001; Salomé & Combes 2003; Hatch et al. 2005; Salomé et al. 2006; Johnstone et al. 2007; Edge et al. 2010; Oonk et al. 2010; Mittal et al. 2011; Werner et al. 2013). Answering the questions of what the origins of these cool ($\sim 10^3 - 10^4$ K) and cold ($< 10^3$ K) gas phases are and how the complex heating and cooling balance in these systems is maintained, requires observations of multiphase material; from synchrotron emitting relativistic plasmas to cold molecular gas and dust.

Groups and poor clusters have shallower potential wells compared with rich galaxy clusters. An important implication of this is that the mechanical output from an active galactic nucleus (AGN) outburst is of the same order as the group binding energy. The effects of AGN feedback in groups may well be different to that observed on the cluster scale. The majority of galaxies in the Universe are situated in group environments. Therefore, investigating the nature of AGN feedback in lower mass systems is paramount to our understanding of galaxy evolution.

The nearby galaxy group, Abell 3581 (Fig. 1, $z = 0.0218$, distance $d = 93.6$ mpc), presents an excellent case study for the investigation of the thermal regulation of groups of galaxies. It has a system temperature of $\sim$1.7 keV (Sun et al. 2009) and hosts the most luminous X-ray cool core among galaxy groups with $z \leq 0.05$. The central AGN, PKS 1404−267, has the highest radio power of any nearby group with a large cool core (e.g. Sun 2009). This cool core co-exists with one of the most spectacular and luminous Hα nebulae observed in galaxy groups, which surrounds the brightest group galaxy (BGG) IC 4374 (Johnstone et al. 1987; Danziger & Focardi 1988). CO(2−1) emission with an intensity of 0.62 ± 0.15 K km s^{-1} ($I_{\rm CO} = \int T \Delta V$) is also detected in the central galaxy. The detection of CO(2−1) was made with IRAM-30 m observations of the nucleus of Abell 3581 (the observations were centred on RA $14^{\rm h}\,07^{\rm m}\,29^{\rm s}.76$, Dec. $-27^\circ\,01'\,05''.9$, J2000) with an 11 arcsec full width half-maximum (FWHM) beam width. The previous *Chandra* observations reported in Johnstone et al. (2005) have shown that two X-ray cavities exist in the centre of the system, where the AGN jets are currently displacing the hot interstellar medium (ISM). Sanders et al. (2010) observed Fe XVII emission lines in the core of Abell

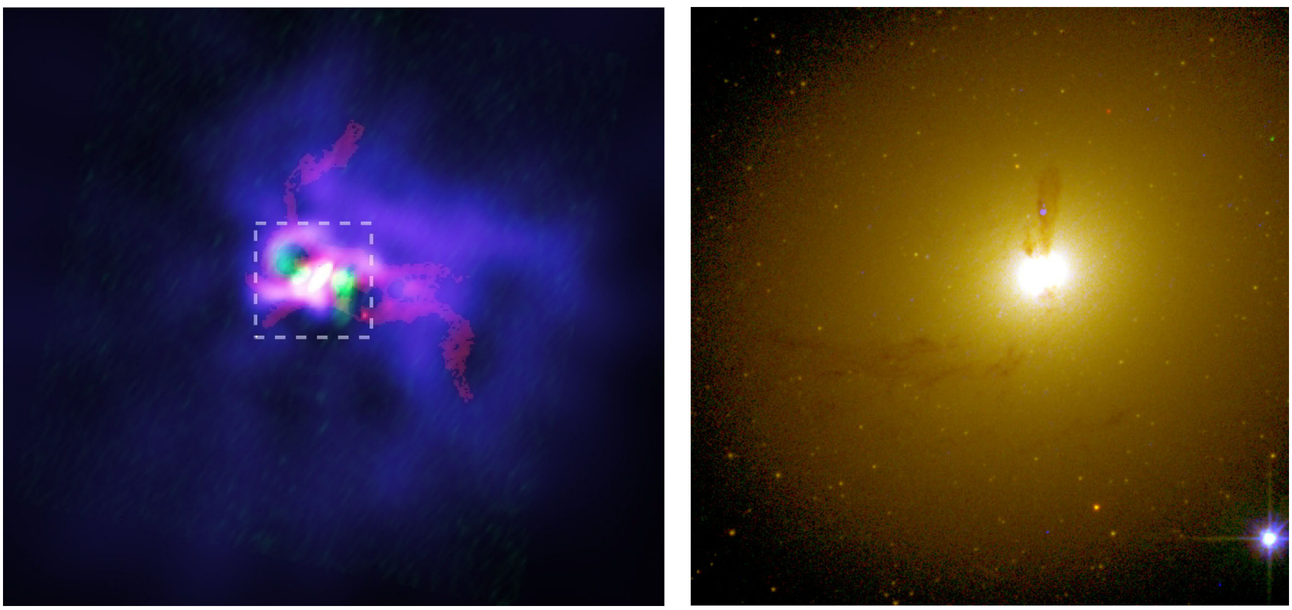

Figure 1. Left: three colour image of Abell 3581 formed from an adaptively smoothed *Chandra* X-ray image with the average at each radius removed (blue), archival VLA 1.4 GHz radio emission (green) and SOAR narrow-band Hα+[N II] image (red). The radio bubbles push aside the hot X-ray gas forming the inner two cavities. Another 'ghost' X-ray cavity is observed to the south-west devoid of radio emission. Filaments of ionized gas encase the young bubbles and are entrained beneath the older cavity. Right: colour composite of the central group galaxy, IC 4374, in the three *HST* filters *F*300*X* (blue), *F*555*W* (green) and *F*814*W* (red). The region shown to the right is highlighted on the left hand figure by the white rectangle which has dimensions 24.2 arcsec (10.5 kpc) across. Dust filaments are observed aligned with the Hα+[N II] and a young star cluster is observed in the dust to the north of the nucleus.

Table 1. Summary of observations.

Telescope	Filter	Exposure	Date	ID	PI
SOAR/SOI	CTIO 6693/76	3×600 s	2008 July 8		Sun/Donahue
	CTIO 6520/76	3×360 s	2008 July 8		
HST/WFC3/UVIS	*F*300*X*	5427 s	2011 February 2	12373	Sun
	*F*555*W*	1335 s	2011 February 2		
	*F*814*W*	1044 s	2011 February 2		
VLT/VIMOS	HRO grism, 0.67 arcsec fibres	4500 s	2009 March 30	082.B-0093(A)	Fabian
JVLA	*L* band, BnA configuration	4 h	2012 September 8	SB0410	Sun
GMRT	610 MHz	2.4 h	2010 May	18-009	Sun
	235 MHz	2.4 h	2010 May		
Chandra/ACIS-S		85 ks	2011 January 3rd	12884	Sun

3581, indicating the presence of low-temperature, 0.5 keV, X-ray emitting gas. The authors find evidence that this X-ray coolest detected gas phase has a low-volume filling fraction (3 per cent) so the cool blobs exist interspersed in the hotter surrounding medium. Such low-volume filling factor cool X-ray gas has been seen in other objects (e.g. Sanders & Fabian 2007; Sanders, Fabian & Taylor 2009; Sanders et al. 2010; Werner et al. 2010, 2013). Sanders et al. (2010) find no evidence for O VII emission lines in Abell 3581 implying very little of the gas can be cooling radiatively below 0.5 keV. Either non-radiative cooling is occurring or a heating source is needed which targets this coolest X-ray gas without overheating the surroundings. Thus, Abell 3581 is an ideal system in which to study AGN heating and the multiphase gas in group cool cores.

In this paper, we present deep multiwavelength imaging and spectroscopy of the central galaxy in Abell 3581 and the surrounding ICM (details of the observations are given in Table 1). Throughout this paper, we assume the standard Λ cold dark matter cosmology where $H_0 = 71\,\mathrm{km\,s^{-1}}$, $\Omega_\mathrm{m} = 0.27$ and $\Omega_\Lambda = 0.73$. For this cosmology and at the redshift of IC 4374 ($z = 0.0218$), an angular size of 1 arcsec corresponds to a distance of 0.435 kpc.

2 OPTICAL DATA

2.1 SOAR

Narrow-band optical imaging was performed with the 4.1 m Southern Astrophysical Research (SOAR) telescope on 2008 July 8 (UT) using the SOAR Optical Imager (SOI). The night was photometric with a seeing of around 1.0 arcsec. The CTIO 6693/76 narrow-band filter was used for the Hα+[N II] lines, and the CTIO 6520/76 filter for the continuum. Three 600 s exposures were taken with the 6693/76 filter and three 360 s exposures with the 6520/76 filter. Each image was reduced using the standard procedures in the IRAF MSCRED package and the spectroscopic standard EG 274. The pixels were binned 2×2, for a scale of 0.154 arcsec per pixel. More details on the SOI data reduction and the continuum subtraction can be found in Sun, Donahue & Voit (2007). The net (continuum-subtracted) Hα image has been published in Sun (2012).

2.2 *HST*

Observations were made using the Wide Field Camera 3 (WFC3) UVIS channel on the *Hubble Space Telescope* (*HST*) on 2011 February 2 in the *F*300*X*, *F*555*W* and *F*814*W* filters. The total exposure times in each filter were 5427, 1335 and 1044 s, respectively. Throughput of the *F*555*W* filter at the redshifted wavelengths of the strong emission lines, Hα+[N II] $\sim$ 6700 Å, is only of the order of a few per cent. Standard procedures were used to bias-subtract and flat-field the data frames, and to drizzle the science frames together, these procedures use the software DRIZZLEPAC and are described in the *HST* WFC3 data handbook.

The optical images are shown in Figs 2–4. No corrections for reddening have been made to the images, although a relative intrinsic $E(B-V)$ image of the galaxy is shown in the right-hand panel of Fig. 4. This reddening map is formed by first correcting the broad-band *HST* imaging for Galactic reddening in the direction of Abell 3581. We take the Galactic reddening to be $E(B-V) = 0.060 \pm 0.001$ using the reddening maps of Schlegel, Finkbeiner & Davis (1998) and assuming the Galactic extinction law of Cardelli, Clayton & Mathis (1989). We then converted the *HST*/WFC3/UVIS broad-band images into AB magnitude units and subtracted the *F*814*W* broad-band *HST* image from the *F*555*W* band. We then subtracted the value at a reference point, within the galaxy, but where there was no evidence for dust lanes in the single *F*555*W* or *F*300*X* frames. The point chosen as our reference is given by the coordinates RA 14$^\mathrm{h}$ 07$^\mathrm{m}$ 29$^\mathrm{s}$.768, Dec. −27° 01′ 05″.20 (J2000). This then provides an $E(F555W - F814W)$ relative intrinsic reddening map.

To convert the map to $E(B-V)$ units requires the assumption of an attenuation curve. We assume the Cardelli et al. (1989) extinction law and calculate A_λ/A_V from the *HST* filters. We use the pivot wavelengths of the *F*555*W* and *F*814*W* filters given in the *HST* WFC3 data handbook as the effective wavelength of the filters. Due to the broad nature of the filters and the low redshift of our object, no *K*-correction is made.

2.3 Integral field spectroscopy

Observations were made on 2009 March 30 using the VIsible Multi-Object Spectrograph (VIMOS) on the Very Large Telescope (VLT) in Cerro Paranal, Chile (see Le Fèvre et al. 2003; Zanichelli et al. 2005 for a description of the VIMOS IFU and a discussion of data reduction techniques). We obtained High Resolution Orange (HRO, $R = 2650$) data using the larger 0.67 arcsec fibres giving a field of view of 27 arcsec × 27 arcsec with 1600 fibres. The wavelength coverage across the whole field of view in the HRO grism is from 5250to7400 Å which covers the redshifted spectral lines of [N I] λ5199 to [S II] λ6731, including the strong spectral lines of [O I] λ6300, Hα and [N II] $\lambda\lambda$6548,6583. However, due to the centring of the pseudo-slits in each quadrant the spectral coverage varies from quadrant to quadrant. The result is that the eastern side of our field of view has an additional coverage of the redshifted

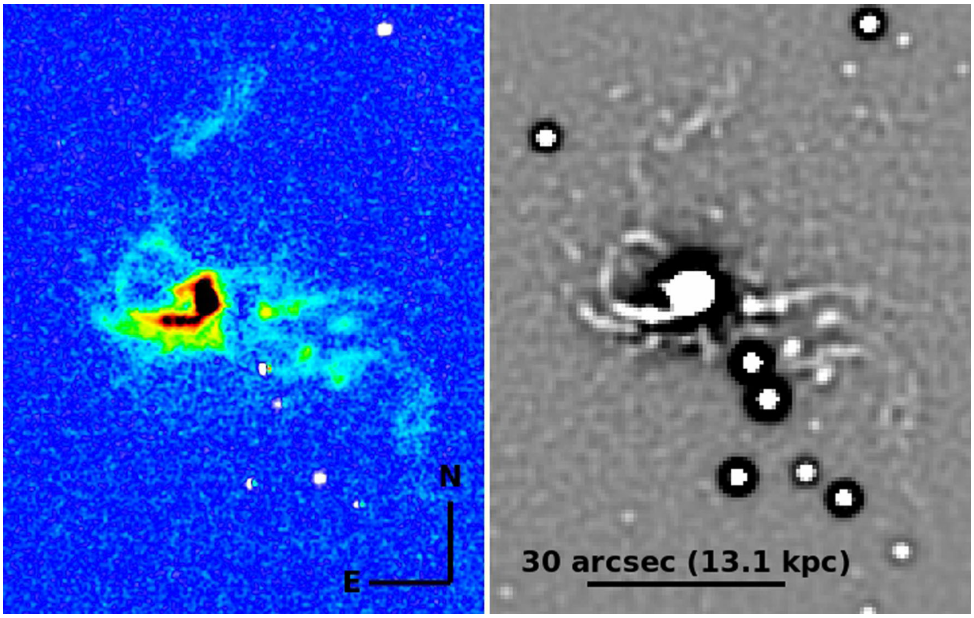

Figure 2. Left: net narrow-band Hα emission image, taken with the SOAR telescope, of the BGG in Abell 3581 after removal of continuum emission with the CTIO 6520/76 filter. Right: the unsharp masked Hα emission image. The initial image has been smoothed by a 2D Gaussian with $\sigma = 1$ arcsec, subtracted from the original and binned by 4 pixels (0.6 arcsec) in each direction.

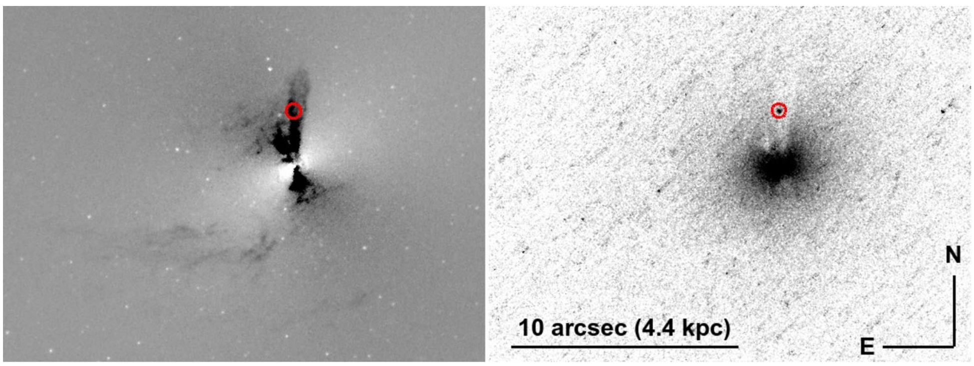

Figure 3. Left: *HST F*555*W* image with a smooth elliptical isophotal model subtracted. The dark feature piercing north–south through the nucleus and turning towards the south-east is absorption from a prominent dust lane. Right: *F*300*X* image of the same region. The red circle shows a young star cluster not seen in the visible (*F*555*W* and *F*814*W*) images. The star cluster coincides with the northern dust lane.

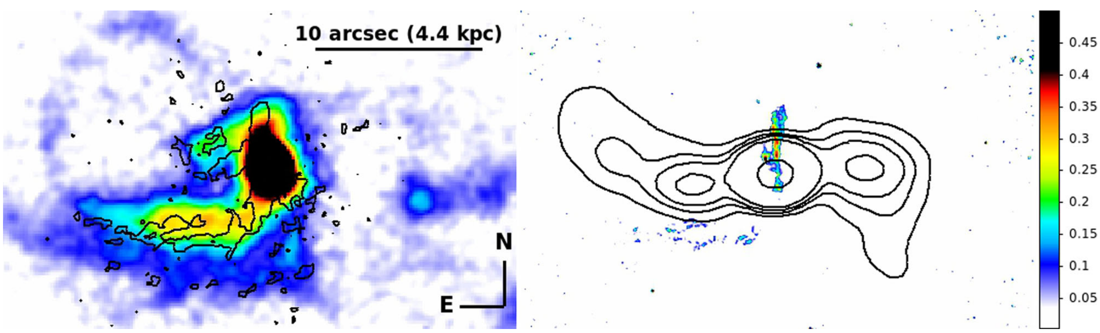

Figure 4. Left: the central region of the net Hα image overlaid with contours of dust absorption. The dust closely coincides with the inner Hα filaments. Right: the relative dust attenuation in the BCG in units of $E(B - V)$ magnitudes after correction for Galactic reddening. Contours of *L*-band Jansky Very Large Array (JVLA) radio emission, which fill the inner X-ray cavities, are overlaid. The angular scale is the same as the left hand panel.

spectral line of [O III] λ5007. The total exposure time of these observations was 4500 s.

The data were reduced by the VIPGI[1] pipeline (see Scodeggio et al. 2005 for a description of VIPGI). The data cubes were combined, transmission corrected, sky absorption and emission corrected and corrected for Galactic extinction ($E(B-V) = 0.060 \pm 0.001$) using a set of IDL routines. The O_2 telluric absorption feature at ∼6800–6900 Å falls over the [S II] doublet and as such warranted special attention. We use observations of two standard stars taken just before and after the science observations to correct for this feature.

Due to the nature of the filamentary system, we choose to bin the data based on the surface brightness of [N II] λ6583 emission, the strongest line observed, using the contour binning technique of Sanders (2006) and binning to a signal-to-noise of 10.

We then fit the emission lines in IDL using MPFIT (Moré 1978; Markwardt 2009). The strong emission lines of [N II] λλ6548,6583 and Hα are fitted simultaneously across the field of view. The redshift and velocity dispersion are constrained to be the same for these emission lines and the integrated flux of the [N II] doublet is tied in the ratio 3:1, the scaling being dictated by the atomic parameters (Osterbrock & Ferland 2006). The [S II] and [O I] lines are fitted separately (the [O I] doublet flux is also tied by atomic parameters); however, the morphology and velocity structure of all emission lines are similar. We fit Gaussians to the spectra with 1 and 2 velocity components and both with and without a broad Hα component. Using MPFTEST in IDL, we determine that a one component velocity structure is sufficient to fit the majority of our data. However, we require a broad Hα component within the inner 2 arcsec^2 radius of the galaxy.

In the images from IFU data, only pixels where the emission lines were detected at a 4σ or greater level are shown. The instrumental spectral resolution is determined from a fit to strong sky emission lines and is found to be 98 $\mathrm{km\,s^{-1}}$ at FWHM.

3 X-RAY DATA

Chandra X-ray data of Abell 3581, with an exposure time of 85 ks, were taken on 2011 January 3 (ObsID 12884). The observations were conducted with the Advanced CCD Imaging Spectrometer (ACIS). The data were reprocessed using the CIAO (Fruscione et al. 2006) ACIS_PROCESS_EVENTS tool, applying the VFAINT processing to lower the non-X-ray background. To look for contaminating flares, we examined the light curve of ACIS CCD 5 between 2.5 and 7 keV in 200 s bins. A sigma clipping algorithm was used to search for flared periods, of which there were none. Standard blank-sky background data sets were used, re-projected to match the observation and with the exposure time adjusted to match the background-dominated 9–12 keV observational count rate. To make the spectral maps, we used the contour binning algorithm (Sanders 2006) to create regions with a signal-to-noise ratio of 20 (around 400 counts). Spectra and background spectra were extracted from these bins, and response and ancillary response regions were created, weighting response regions by the number of counts in the 0.5–7 keV band. We fitted the spectra in XSPEC between 0.5 and 7 keV, minimizing the modified C statistic. We used the APEC thermal model to fit the spectrum (Smith et al. 2001), with Galactic absorption ($4.36 \times 10^{20}\ \mathrm{cm^{-2}}$) applied. In the fits, the temperature, metallicity and normalization were allowed to vary.

In order to examine the surface brightness edges in the images, we fitted and subtracted a double-β model, using the SHERPA fitting package, to an azimuthally averaged, background-subtracted surface brightness profile, centred on and extracted between a radius of 2.5 and 120 arcsec. The surface brightness profile is from the exposure-corrected image with point sources removed manually. The image is in the energy range 0.5–7 keV. Despite the asymmetry of the cluster, the model fits the data reasonably well. However, deviations from the fit are seen at ∼50 arcsec, ∼80 arcsec and in the central 20 arcsec. These deviations correspond to surface brightness edges which will be examined further in Section 5.2. Double-β fits to individual sectors and empirical azimuthally averaged profiles are also fitted and removed from the surface brightness images to highlight substructure.

For the temperature and density profiles across the 'bubble' and 'cold front' (see Section 5.2), we extracted spectra from the regions of interest, and fitted the spectrum within XSPEC (version 12.8.0a[2]) with an absorbed MEKAL model. The regions for the spectral analysis were chosen such that there were at least 3000 counts in each bin. Only data in the 0.5–7.0 keV range were used. C statistics were used for the fit and spectra were deprojected using the routine developed in Sanders & Fabian (2007) and Russell, Sanders & Fabian (2008). The Galactic absorption in the direction of Abell 3581 was taken as $4.36 \times 10^{20}\ \mathrm{cm^{-2}}$, using the value of Kalberla et al. (2005) and was frozen in the fits. The solar photospheric abundance table by Anders & Grevesse (1989) was used in the spectral fits. Error bars on the temperature, density and pressure plots are shown at the 90 per cent level.

4 RADIO DATA

4.1 JVLA

High-frequency radio observations of Abell 3581 were obtained with the NRAO[3] Jansky Very Large Array (JVLA; Perley et al. 2011) at *L* band (1–2 GHz). Due to the low declination of the target, the observations were undertaken in the hybrid BnA configuration on 2012 September 08 (project ID: SB0410). The extended north arm of the hybrid configuration allows for a more circular beam for the target. The observations were a total of 4 h and were taken with two 512 MHz wide basebands centred at 1314 and 1686 MHz. We configurated the WIde-band Digital Architecture (WIDAR) correlator so that each baseband had 8 subbands with 64 channels per subband for a frequency resolution of 1 MHz. We used 3C 286 as our absolute flux and bandpass calibrator and J1351−1449 as our phase calibrator.

The data were flagged and calibrated using NRAO's Common Astronomy Software Applications (CASA[4]) data reductions package. We Hanning smoothed the data to reduce the effects of Gibbs ringing around strong radio frequency interference (RFI) which is common at *L* band. We then flagged the data in the time and frequency domains to remove the majority of the significant RFI. Additional time-domain flagging on the bright calibrators was done using the

[1] VIMOS Interactive Pipeline Graphical Interface (VIPGI), obtained from http://cosmos.iasf-milano.inaf.it/pandora/

[2] We used the AtomDB 2.0 release which includes changes to the iron L-shell data affecting $kT < 2$ keV plasma which has the effect of increasing the temperature (10–20 per cent) while decreasing the abundances (∼20 per cent) when compared with AtomDB 1.3.1.

[3] The National Radio Astronomy Observatory is a facility of the National Science Foundation operated under cooperative agreement by Associated Universities, Inc.

[4] http://casa.nrao.edu

average calibrator amplitudes. We used all calibrators to calculate the parallel hand group delays and applied the results to all sources. We then followed standard techniques for bandpass calibration, taking into account the spectral index of the bandpass calibrator, as well as gain calibration. Following calibration, we split off the target field and undertook additional flagging before imaging the data with MFS algorithm in CASA which allows us to deal with the wide-band data. We applied four rounds of phase only self-calibration on the target followed by a round of amplitude and phase self-calibration. The final image of Abell 3581 has a noise of $\sigma = 22\,\mu$Jy beam^{-1} with a resolution of 2.56×2.07 arcsec at a position angle of $-84.°95$.

4.2 GMRT

Abell 3581 was observed with the Giant Metrewave Radio Telescope (GMRT) at 235 MHz and 610 MHz (project 18-009) in 2010 May, for approximately 3 h, including calibration overheads. The observations were made using the dual-frequency mode. The 610 MHz data were collected using the upper and lower side bands (USB and LSB) with an observing bandwidth of 16 MHz each. Only the USB was used at 235 MHz, with a bandwidth of 8 MHz. We chose the default spectral-line observing mode, with 128 channels for each band at 610 MHz (64 channels at 240 MHz) and a spectral resolution of 125 kHz/channel. The data sets were calibrated and reduced using the NRAO Astronomical Image Processing System package (AIPS) as described in Giacintucci et al. (2011). Self-calibration was applied to the data to reduce residual phase variations and improve the quality of the final images. Due to the large field of view of the GMRT at low frequencies, we used the wide-field imaging technique at each step of the phase self-calibration process, to account for the non-planar nature of the sky. The final images were produced using the multiscale CLEAN implemented in the AIPS task IMAGR, which results in better imaging of extended sources compared to the traditional CLEAN (e.g. Wakker & Schwarz 1988; Cornwell, Holdaway & Uson 1993). The full resolution of our final images is 8 arcsec × 4 arcsec at 610 MHz and 16 arcsec × 11 arcsec at 235 MHz. The rms noise level (1σ) in these images is 0.1 and 0.9 mJy beam^{-1}, respectively. Residual amplitude errors are within 8 per cent at 240 MHz and 5 per cent at 610 MHz.

5 RESULTS

5.1 Optical

5.1.1 Morphology

The BGG in Abell 3581 has a smooth, relaxed appearance in broad-band optical images. However, the narrow-band Hα+[N II] image shows striking filaments of ionized gas. These filaments connect to the nucleus in the easterly and westerly directions, parallel to the current radio axis, then curve sharply towards the north and south, respectively (see Fig. 2). In the easterly direction, the filaments arc round and apparently encase one of the previously detected X-ray bubbles. The filament system is complex, formed of at least a few strands in each direction and is not one continuous structure. Filaments of this nature have now been observed in many massive galaxies dominating the centres of X-ray bright cool-core groups and clusters. Our VLT VIMOS IFS data show the emission lines of Hα, [N II], [S II] and [O I] in the inner filament all share the same morphology.

A dust lane stretching north to south through the nucleus is clearly visible in all optical bands and in the *F*300*X* image. Fig. 3 shows the *F*555*W* image with the smooth elliptical component subtracted, highlighting the myriad dust lanes. The nuclear component of the dust lane is ∼5 arcsec in length and extends radially in two plume-like structures; one to the north and one to the south. In the south, beyond a few arcsec, the dust lane abruptly changes direction and traces the ionized gas filament to the east (see Fig. 4). The dust extends at least 10 arcsec along the filament; whether the dust stops here or continues all the way along the filament is unknown. A similar extension to the east is seen in the dust emission north of the nucleus. Contours of the dust emission are overlaid on the net Hα+[N II] image in the left-hand panel of Fig. 4. A young star cluster is found coincident with the northern dust lane but no other obvious young stellar structures are observed in the filaments.

The right-hand panel of Fig. 4 shows an $E(B - V)$ map of the relative intrinsic extinction in the central galaxy due to the dust lanes; the reddening due to absorption by dust is significant in the central galaxy. This is overlaid with contours of the JVLA *L*-band radio emission from the inner X-ray cavities (Johnstone et al. 2005). The dust lane in the south and extending towards the east of the nucleus also coincides also with the outer edge of the radio bubble.

5.1.2 Nebula kinematics

Our VIMOS IFS data (Fig. 5) provide evidence that a broad Hα emission line is necessary in the central 22 pixels, a region ∼2 arcsec in radius (∼3 pixels or ∼1 kpc radius) and coinciding with the largest surface brightness of high-frequency radio emission. Our PSF is ∼2.1 pixel FWHM so the emission should be resolved. The broad-line region of the AGN is expected to be significantly smaller than this, being typically <0.1 pc or for the most luminous quasars ∼0.25 pc. This broad component has a best-fitting line-of-sight

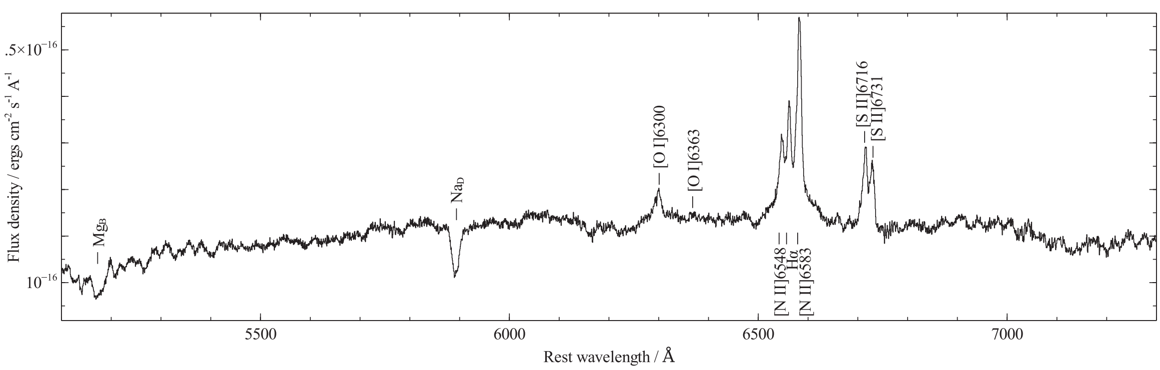

Figure 5. The optical spectrum of the BGG nucleus in Abell 3581.

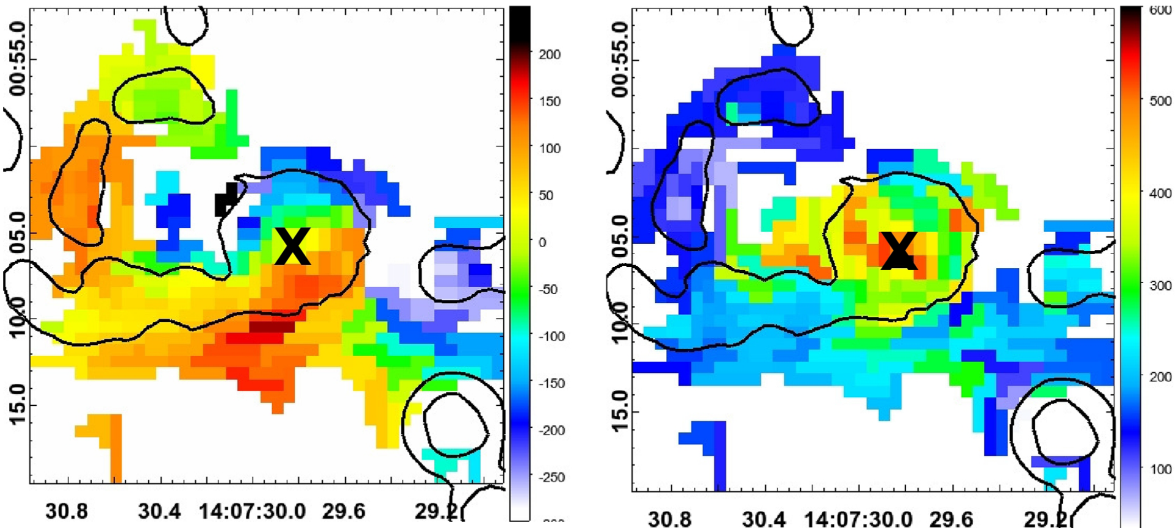

Figure 6. The line-of-sight velocity of the narrow line component of the optical nebulosity (left) from a fit to the strong [N II] λ6583 line and the FWHM velocity width (right) after correction for the instrumental resolution (98 km s^{-1}, FWHM). Colour bars are in units of km s^{-1} and the velocity zero-point is taken to be 6450 km s^{-1}, the velocity of the Hα nebulosity at the position of the nucleus ($14^{h}07^{m}29\overset{s}{.}8$, −27° 01′ 06″.4, marked with an X). Only pixels where the [N II] λ6583 emission line was detected above 4σ are shown and the images are overlaid with contours of Hα emission from our SOAR narrow-band images.

velocity redshifted ∼150 km s^{-1} with respect the narrow Hα emission-line component within the same region. The breadth of the line is ∼2900 km s^{-1} and the Hα flux of the broad component in the inner 2 arcsec radius is $2.21 \pm 0.03 \times 10^{-14}$ erg cm^{-2} s^{-1}.

The line-of-sight velocity and velocity width of the narrow component of the ionized gas nebulae is shown in Fig. 6. The units of both figures are km s^{-1} and the line-of-sight velocity zero-point is taken to be the nucleus ($14^{h}07^{m}29\overset{s}{.}8$, −27° 01′ 06″.4) as determined from the *L*-band JVLA radio images. Overlaid are the contours from the narrow-band Hα image. A smooth line-of-sight velocity gradient is observed through the nucleus, perhaps indicative of rotation or an outflow. We note that no evidence for rotation of the stellar component, observed through the NaD absorption line, is seen.

The gradient observed in the galaxy core extends smoothly along the filament, and around the arc encasing the inner bubble, consistent with a common origin of the filament gas and the gas in the core. The velocities are low in the filaments with line-of-sight velocities of ∼50 km s^{-1} and velocity dispersions of ∼150 km s^{-1}. The kinematics are therefore very similar to those observed in filament systems surrounding other BCGs (e.g. Hatch et al. 2005; Canning et al. 2011).

5.1.3 Emission-line fluxes and ratios

Our HRO data span the redshifted spectral range of [N I] λ5199 to [S II] λ6731 across the whole field of view and the redshifted spectral range of [O III] λ5007 to [S II] λ6731 in the south-east and north-east quadrants. These data are fitted within IDL as described in Section 2.3. At the resolution of our observations, all emission lines detected in our data have the same spatial morphology and, aside from the nuclear region, our data are not of sufficient spectral resolution to constrain more than one velocity component.

We check the fluxes in Hα between our net Hα image and our VIMOS IFU in a region on the inner south-east filament. The region is of size 19.5 × 23 arcsec centred on $14^{h}\,07^{m}\,30\overset{s}{.}2$, −27° 01′ 04″.8. Our fluxes are 5.1×10^{-14} and 5.7×10^{-14} erg cm^{-2} s^{-1} in the narrow-band image and IFU image, respectively. The fluxes agree within ∼10 per cent. The error on the integrated flux from our IDL fit ∼7 per cent and a 1 per cent continuum flux variation between the ON/OFF filter images translates to ∼10 per cent net flux change for A3581. Our fluxes are therefore consistent.

The left-hand plot of Fig. 7 shows the ratio of the strong [N II] λ6583 emission line to the narrow component of the Hα emission. In the centre of the galaxy, this is observed to peak at the nucleus and to drop radially with distance from the AGN. Farther out on to the filaments the ratio is approximately unity. On the 'inside' of the filaments, the side closest to the radio emission, a larger ratio of [N II] to Hα emission is observed.

The [O III] λ5007 emission line can only be observed in the eastern quadrants of the data cube; we have no information about the [O III] λ5007 emission in the nucleus (right-hand panel of Fig. 7). The [O III] λ5007 emission is over three times stronger in the easterly extension to the north of the nucleus, where the velocity widths are very high, compared to the southern-most regions of the easterly filament. A gradient of [O III] λ5007/Hα emission, similar to that observed in the [N II] λ6583/Hα ratio discussed above, is observed across the more southern filament. The collisional line emission is enhanced relative to the recombination line emission on the 'inside' of the filament and close to the nucleus.

Unusually strong emission lines of [N I] λ5199, characteristic of the filament emission in BCGs, are detected in the extended filaments but no evidence is found for such emission in the nucleus (see Table 2), we also detect He I emission in the extended filaments. We do not observe any evidence for coronal emission lines (emission lines with excitation temperatures of 10^5–10^6 degree gas) in our IFS data. Table 2 gives emission-line ratios compared to Hα for the three regions shown by crossed on Fig. 7. These are the nucleus, the north-easterly extension and farther out on the south-easterly extension. It is quite apparent that these ratios are different due to the comparative importance of various excitation mechanisms in these regions; this highlights the complicated nature of distinguishing excitation mechanisms in the central regions of BGGs/BCGs.

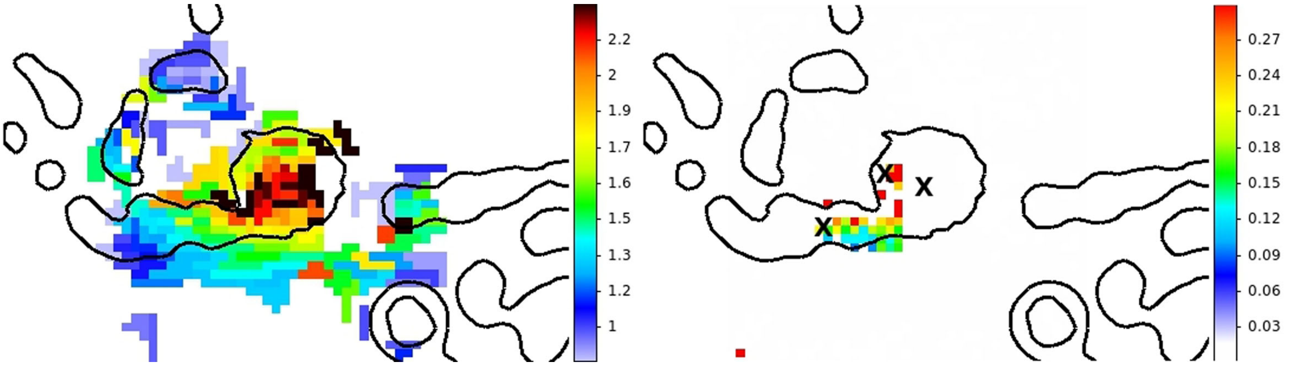

Figure 7. Left: [N II] λ6583/Hα ratio map of the filaments surrounding the two inner bubbles. The ratio is highest in the centre of the galaxy and smoothly drops at larger radius. A spur of high [N II] over Hα emission is also seen north-west of the centre where the velocity dispersion in the gas is larger. Right: the [O III] λ5007/Hα ratio map on the same spatial and intensity scale as the right-hand image. The ratios are corrected for Galactic extinction but no correction for internal extinction has been made. The three crosses indicate regions (the nucleus, NE and SE) where spectra were extracted and the emission-line fluxes detailed in Table 2 and the images are overlaid with contours of Hα emission from our SOAR narrow-band images.

Table 2. Emission-line fluxes (upper panel) and ratios (lower panel) in the three regions indicated by a cross on Fig. 7. Each region was 2 pixels ($\sim$1.3 arcsec) in radius. The units for the fluxes are $\times 10^{-15}$ erg cm^{-2} s^{-1}. [1]Errors in nucleus large – probably due to multiple components. [2]Spectral coverage of VIMOS quadrants is uneven so [O III] λ5007 emission can only be probed to the east of the nucleus. [3]Broader line than Hα due to not being able to resolve the doublet emission.

Emission line	Nuc[1]	SE	NE
Redshift	0.021 695 ± 6E−6	0.021 746 ± 1E−6	0.020 32 ± 3E−5
Velocity width	301 ± 6	209 ± 1	355 ± 36
[O III] λ5007	N/A[2]	0.4 ± 0.02	0.4 ± 0.02
[N I] λ5199	–	0.3 ± 0.05[3]	0.09 ± 0.02[3]
He I 5875	–	0.1 ± 0.02	–
[O I] λ6300	1.7 ± 0.4	0.7 ± 0.01	0.2 ± 0.03
[O I] λ6363	–	0.2 ± 0.02	–
[N II] λ6548	2.7 ± 0.1	1.5 ± 0.04	0.3 ± 0.01
Hα 6563	4.6 ± 0.1	3.1 ± 0.01	0.6 ± 0.03
[N II] λ6583	11.4 ± 0.07	4.5 ± 0.02	1.1 ± 0.03
[S II] λ6717	3.2 ± 0.2	1.5 ± 0.02	0.6 ± 0.02
[S II] λ6731	3.0 ± 0.2	1.2 ± 0.03	0.4 ± 0.1
Line/Hα			
[O III] λ5007	N/A[2]	0.13	0.67
[N I] λ5199	–	0.10	0.15
He I 5875	–	0.03	–
[O I] λ6300	0.37	0.23	0.33
[O I] λ6363	–	0.06	–
[N II] λ6548	0.59	0.48	0.5
Hα 6563	1.0	1.0	1.0
[N II] λ6583	2.48	1.45	1.83
[S II] λ6717	0.70	0.48	1.0
[S II] λ6731	0.65	0.39	0.67

5.1.4 *Star formation*

A young star cluster is observed, projected on the dust lane, 2.5 arcsec north of the nucleus (see Fig. 3). No other young clusters are observed in the filament system. Using our relative reddening map, and assuming the intrinsic dust is an obscuring screen, we correct the observed fluxes in the broad-band filters and determine the emission from the young star cluster. Using a GALEV evolutionary synthesis model (Kotulla et al. 2009) for a simple stellar population the *F*300*X*–*F*555*W* and *F*300*X*–*F*814*W* colours indicate an age $<10^8$ yr and a mass $\sim 10^4$ M$_\odot$.

Abell 3581 has not been observed by *Spitzer*. However, the central galaxy is detected in all four *WISE* bands. The *WISE* All-Sky Source Catalog, measures an extrapolated flux at 24 µm as 8.0 mJy. Using equation 10 of Rieke et al. (2009), and assuming a Kroupa (2002) initial mass function (IMF), indicates the star formation rate (SFR) in the central galaxy is $\sim$0.21 M$_\odot$ yr^{-1}. The near- and far-ultraviolet emission from *GALEX* indicates 0.3 and 0.1 M$_\odot$ yr^{-1} (these values assume no intrinsic reddening correction).

The net Hα image of IC 4374 is shown in Fig. 1. The total Hα flux is 6.9×10^{-14} erg cm^{-2} s^{-1}, assuming [N II]6583/Hα = 1.5 and [N II]6548/[N II]6583 = 1/3 (an average from our VIMOS IFS data – we note that this does not cover the entire extent of the filament system). If the nucleus is excluded (a circle with a radius of 2.5 arcsec), the total flux is 4.8×10^{-14} erg cm^{-2} s^{-1}. Using the Kennicutt (1998) relation, SFR (M$_\odot$ yr^{-1}) = 7.9×10^{42} ($L_{\mathrm{H}\alpha}$ / erg s^{-1}), the SFR is $\sim$0.4 M$_\odot$yr^{-1}, assuming no intrinsic extinction for the Hα emission. This is similar to the mass deposition rate in the cool X-ray gas (0.4 M$_\odot$ yr^{-1}; Sanders et al. 2010); however, no UV emission is observed in the filaments.

5.2 X-ray

5.2.1 *Morphology*

The X-ray surface brightness, temperature and metallicity maps are shown in the core in Fig. 8 and on a larger scale in Fig. 9. New outer structures are indicated in Fig. 10. As previously noted by Johnstone et al. (2005), who examined a 7165 s *Chandra* ACIS-S observation of Abell 3581, an X-ray emitting point source lies in the nucleus and two inner cavities exist; one to the east and one to the west of the nucleus. These inner cavities coincide with relativistic synchrotron emitting gas observed as radio bubbles in 1.4 GHz radio emission. The power in these inner 1.4 GHz radio bubbles is 2.5×10^{23} W Hz^{-1} (Johnstone et al. 2005).

Fig. 8 reveals that the low-volume filling, soft X-ray gas, detected by Sanders et al. (2010), lies in filaments. There is excellent spatial correspondence between the coolest, highest density X-ray emitting gas and the Hα emitting filaments. Clear structures are seen in the temperature and metallicity maps suggesting little mixing is occurring in the centre of Abell 3581.

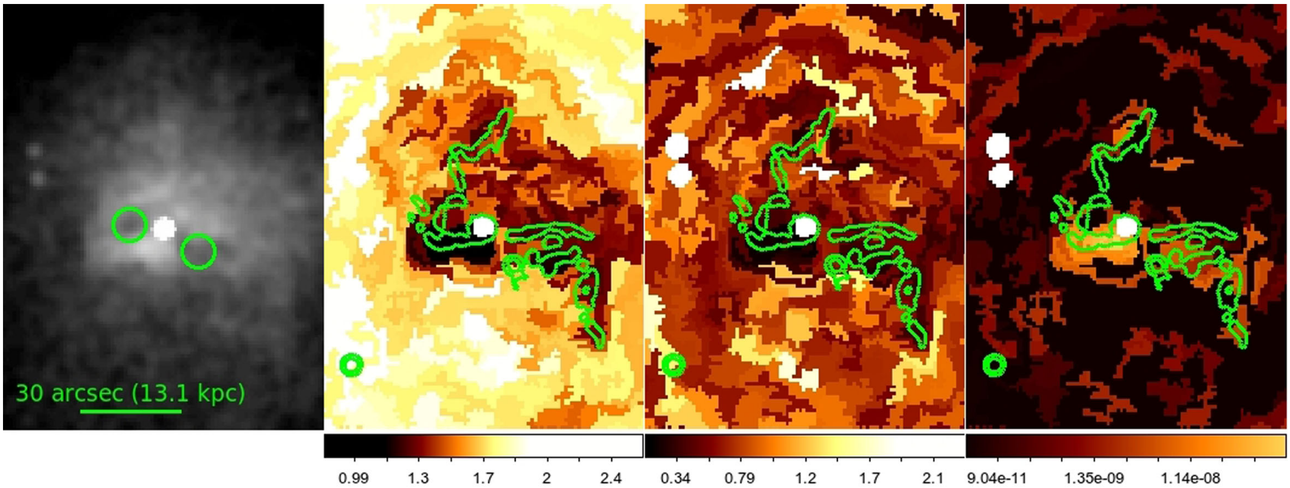

Figure 8. From left: X-ray surface brightness image, X-ray temperature map, X-ray metallicity map and 0.5 keV emission measure map. The inner two depressions corresponding to the regions in which 1.4 GHz radio emission is seen are circled on the X-ray surface brightness image. Contours of Hα emission are overlaid on the temperature, metallicity and emission measure maps. The colour bars are in units of keV, $Z_{\odot}$ and cm^{-5} arcsec^{-2} , respectively.

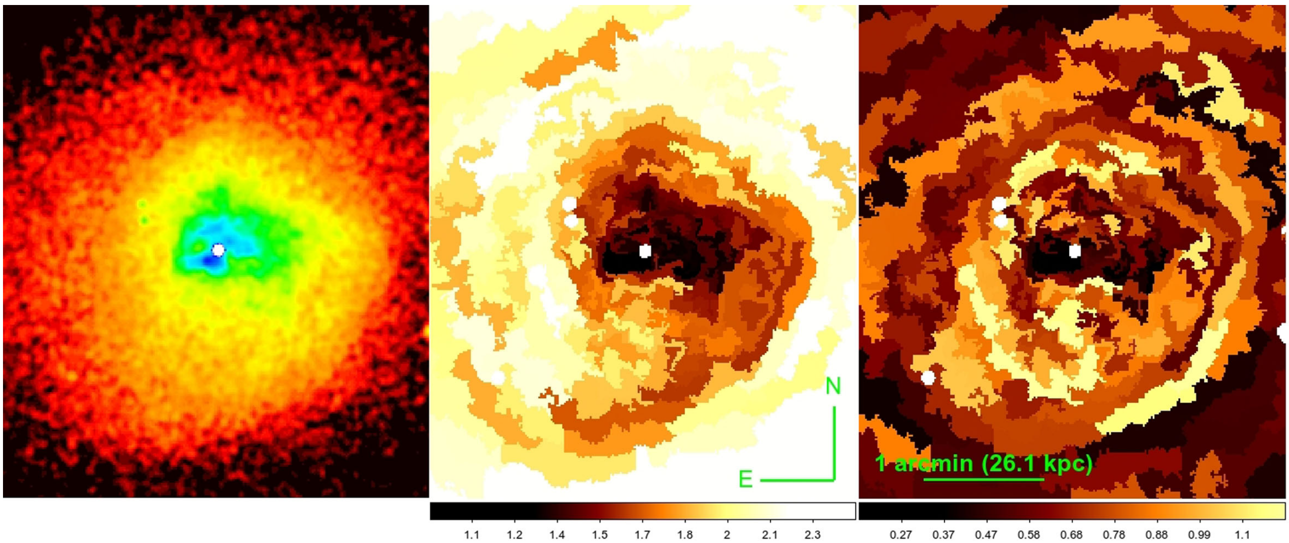

Figure 9. From left: X-ray surface brightness image, X-ray temperature map and X-ray metallicity map. Two depressions are observed which coincide with the 1.4 GHz radio emission in the nucleus, an outer cavity is observed towards the south-west beyond a sharp temperature and metallicity edge and a further surface brightness discontinuity, a likely cold front, is observed beyond this outer bubble. There is an apparent metallicity drop towards the centre, as seen in other similar objects, this could indicate the need for additional temperature components to the model (see discussion in Section 5.2.2).

Additional structure is observed outside of the filaments; surface brightness edges to the east and south indicate two bays where a dearth of X-ray emission could be a signature of outer bubbles (see Fig. 10, white ellipses). An additional X-ray cavity (green ellipse), detached from the nucleus and not observed before, is seen ∼45 arcsec to the west of the nucleus. We do not observe any radio emission, in our frequency bands, coincident with the depression in the X-ray image. The cool X-ray gas is observed to extend up to the new outer bubble but not farther. A clear edge is seen in both maps at the inner edge of the bubble.

The large-scale structure in the X-ray image shows a spiral surface brightness discontinuity (red curve) which wraps around the nucleus in a clockwise direction. The X-ray gas is cooler, denser and higher metallicity within this structure and the entropy, defined as $K = k_B T / n_e^{2/3}$, is lower than the surrounding gas, similar to the gas in the X-ray cool core and may be gas stripped from there by sloshing motions in the core. Fig. 11 shows the X-ray properties through a sector centred on the nucleus and intersecting part of the spiral structure.

5.2.2 *X-ray metallicity*

The X-ray metallicity maps (Figs 8 and 9) show a high-abundance spiral structure but a low-abundance core to the galaxy. Most cool-core galaxy clusters and groups tend to show a central abundance peak (e.g. De Grandi & Molendi 2001). However, an offset peak and metal-enriched spiral is also observed in the Centaurus cluster (Sanders & Fabian 2002), Ophiuchus Cluster (Million et al. 2010) and HCG 62 (e.g. Gu et al. 2007; Gitti et al. 2010; Rafferty et al. 2013). HCG 62 has a central iron abundance of ∼0.3 $Z_{\odot}$ which rises to solar at 20–30 arcsec (5.6−8.4 kpc) before dropping father out (Rafferty et al. 2013) while Centaurus has a central iron abundance

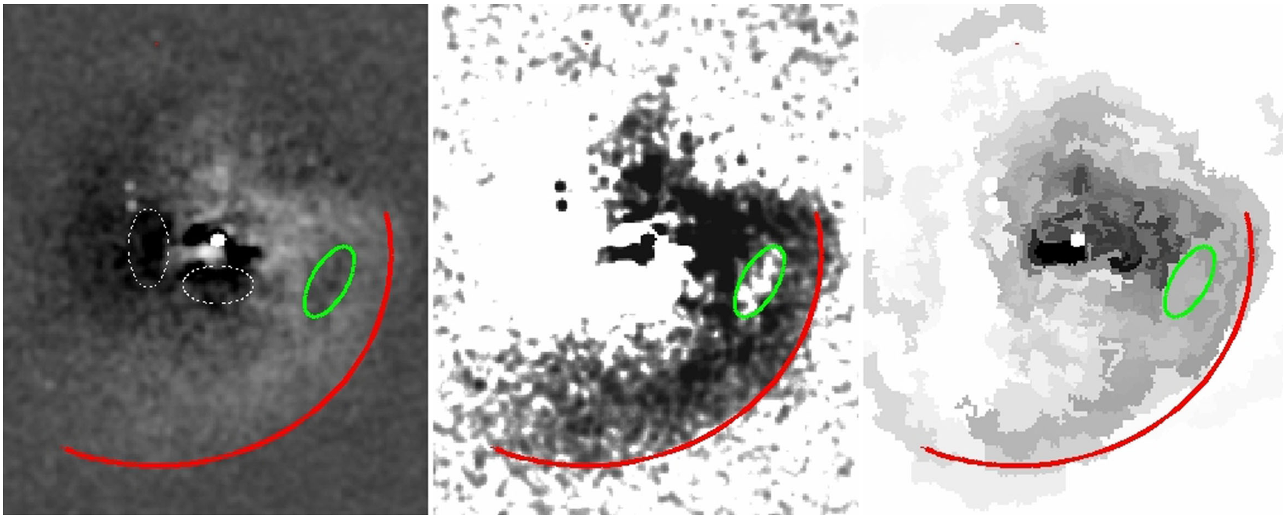

Figure 10. The outer features. Left: unsharpmasked *Chandra* X-ray image of Abell 3581. An image, smoothed with a Gaussian with $\sigma = 25$ pixels has been subtracted from the original. The outer cavity is highlighted in green and the cold front in red. The two 'bays' to the east and south are indicated with dashed white ellipses. Middle: the X-ray surface brightness image after a smooth elliptical isophotal model was subtracted from the original data. The intensity scale was chosen to highlight the outer cavity and spiral. Right: the same regions overlaid on the X-ray temperature map.

of $\sim$0.4 $Z_{\odot}$ rising to $\sim$1.3 $Z_{\odot}$ 15 kpc from the nucleus (Sanders & Fabian 2002). Similarly, with a single-temperature fit to the data, we find an iron abundance of $\sim$0.3 $Z_{\odot}$ in the central regions of Abell 3581 which rises to 0.8–1.0 $Z_{\odot}$ at a distance of $\sim$30−60 arcsec (13.5−26 kpc) coinciding with the spiral structure. The metallicity then drops farther out into the ICM.

Resonance scattering can affect the measured abundances in clusters and groups; however, the effect has not been able to fully explain the metallicity drops (e.g. Mathews, Buote & Brighenti 2001; Gastaldello & Molendi 2004; Sanders & Fabian 2006). A discussion on the effect of low mass X-ray binaries on the derived spectral properties is given in David et al. (2009, 2011). The gas in groups and clusters, viewed in projection, is certainly multiphase and another possibility for the metallicity drop in the central regions of the galaxy may be that a single-temperature model is inadequate in representing the data.

To examine whether the metallicity drop is due to the misrepresentation of a multiphase gas, we fit two temperature VAPEC models within XSPEC (version 12.8.0a) to the X-ray emission in four regions within the cluster. These regions are shown in Fig. 12 and the results of the fit are given in Table 3. The minimum counts in our regions are 5400 counts with two of the regions having greater than 12 000 counts. The results of Table 3 show that the addition of a second temperature component in regions 1 and 2 significantly alters the abundances removing any evidence for a metallicity drop in the central regions. The spiral (region 3) has a similar best-fitting metallicity as the core while beyond the spiral (region 4) the metallicity declines.

5.2.3 *Bubble energetics*

To determine the energetics of the new outer cavity we fit an elliptical isophotal model to the cluster and subtract the median surface brightness at each radius. We then identify, by examining cuts through the resulting surface brightness image, an ellipse representing the cavity.

We define a sector of the cluster centred on the nucleus and extending between the edges of the ellipse (see Fig. 13) up to a radius of 100 arcsec (44 kpc). We create annular regions within this sector. The width of each annulus is determined to be the width necessary to enclose at least 3000 counts; we do this to ensure a good fit to the spectrum. The inner 3 pixels are not used to avoid including the point source. We then fit both the projected and deprojected spectra within XSPEC (as described in Section 3).

Estimating errors on energetics from cavities is fraught with difficulties due to inferring a three-dimensional shape for the bubble from a projected two-dimensional image, not knowing the inclination of the rise direction to the observer, the 'fuzzy' edges of the bubble decrement and due to the shape of the overlying surface brightness profile of the cluster. The errors estimated and quoted in the following sections use the technique of O'Sullivan et al. (2011). Using this technique, the line-of-sight depth is equal to the semiminor axis and the uncertainty on the volume is given by assuming a minimum depth of half this value and a maximum equal to the semimajor axis. However, for the outer cavity, it must be noted that the length of the bubble in a direction perpendicular to the rise direction is given by the semimajor, not semiminor axis of the ellipse; the errors quoted are unlikely to be reliable.

The temperature, density, pressure and entropy profiles in the gas in this sector are shown in Fig. 13. At the position of the X-ray cavity (indicated by a green solid line) we detect a clear jump in the deprojected temperature and a corresponding drop in the density. There is no significant change in the pressure which could indicate that the jump in temperature is due to the gas in the region around the bubble and not the outer layers of the cluster seen in projection with the cavity. However, the errors on the pressure are not constraining.

We estimate the energy in the outer cavity using,

$$E_{\text{bubble}} = \frac{\gamma}{\gamma - 1} PV, \tag{1}$$

where $\gamma = 4/3$ for a relativistic fluid, V is the volume of the cavity and P is the thermal pressure of the ICM, as described in Bîrzan et al. (2004) and Dunn, Fabian & Taylor (2005). The volume of the bubble is derived making the implicit assumption that the bubble is a spheroid, two of whose axes are in the plane of the sky, with a plane of symmetry perpendicular to the rise direction. The ellipsoid volume $V = (4/3)\pi R_1 R_2^2$, where $R_1 = 3.8$ kpc (8.8 arcsec)

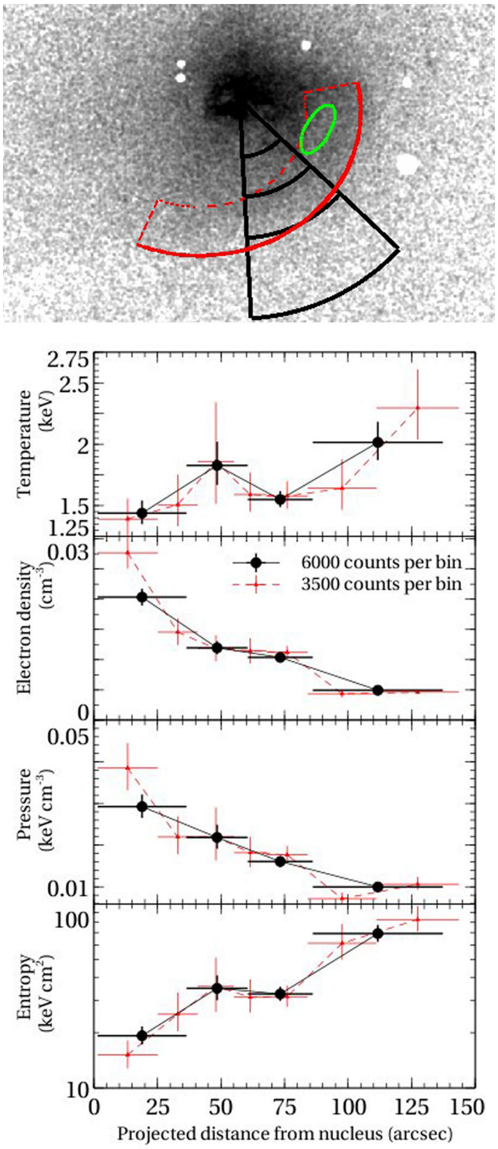

Figure 11. Deprojected profiles showing the temperature, density, pressure and entropy of a sector centred on the cool core and intersecting the spiral. The entropy and temperature of the gas in the spiral is lower than that of the gas between the spiral and the core. The black regions contain 6000 counts and are shown on the above plot with the outer bubble, spiral cold front and approximate width of the spiral also shown. The red regions contain 3500 counts such that the statistics remain good while allowing two regions on the spiral.

is the length of the projected ellipsoid axis in the direction of the nucleus, in this case the semiminor axis of the ellipse, and $R_2 = 8.4$ kpc (19.3 arcsec) is the length of the ellipsoid in a perpendicular direction, here given by the semimajor axis of the ellipse. Using this formalism, $E_{\rm bubble} = 5.5(2.7-11.8 \times 10^{56})$ erg. A similar treatment gives the energy in the inner cavities as $E_{\rm bubble} = 2.4(1.2$–$2.9 \times 10^{56})$ erg, assuming $R_1 = 3.6$ kpc (8.4 arcsec) and $R_2 = 3.0$ kpc (6.9 arcsec). Diehl et al. (2008) estimate similar energies for these inner bubbles with values of 3.49×10^{56} and 3.37×10^{56} for the inner bubble energies.

The outer bubble rise time as measured by the sound speed, buoyancy and refilling time-scales (Churazov et al. 2000; McNamara et al. 2000; Blanton et al. 2001) are 3, 4 and 5×10^7 yr,

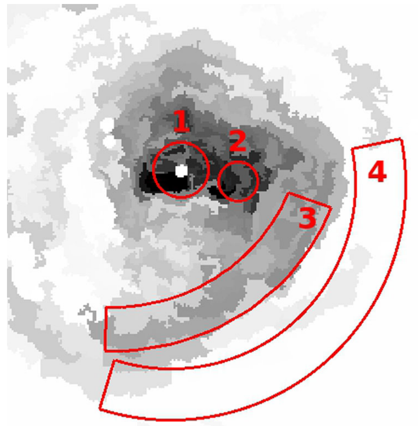

Figure 12. Regions 1–4 where the X-ray spectra has been extracted and a multitemperature gas is fitted to the data. The point source in region 1 has been removed. The results of the single-temperature and two-temperature fits are given in Table 3.

respectively, and for the inner bubbles are and 0.7, 2 and 6×10^7 yr. Assuming that the sound speed time-scale for the inner bubbles and the buoyancy time-scale for the outer bubble the cavity powers are $P_{\rm x\text{-}cav} = 4.4 \times 10^{41}$ erg s^{-1} for the outer cavity and $P_{\rm x\text{-}cav} = 1.1 \times 10^{42}$ erg s^{-1} for the inner cavities. A simple scaling from the power in the 1.4 GHz radio emission (2.5×10^{23} W Hz^{-1}), using the relation derived by Cavagnolo et al. (2010), gives $P_{\rm cav} = 3.7 \times 10^{43}$ erg s^{-1} for the inner cavities.

The point source removed X-ray luminosity, between 0.5 and 7 keV, in a circle of radius 9.4 kpc (21.5 arcsec) which encompasses the inner bubbles, a circle of radius 28.3 kpc (65.0 arcsec) which encompasses the outer bubble and the 'cooling radius' (assumed to be where $t_{\rm cool} < 7.7$ Gyr, $r_{\rm cool} \sim 57$ kpc; Sanders et al. 2010), corrected for Galactic absorption are 2.1×10^{42}, 7.8×10^{42} and 1.1×10^{43} erg s^{-1} , respectively.

5.3 Radio

5.3.1 Morphology

The morphology of the radio emission is shown in Fig. 14. The high-frequency 1.4 GHz emission fills the inner cavities; these are surrounded by the ionized gas nebulae which coincides with the lowest temperature X-ray emission. This is consistent with the inflation of the bubbles leading to the displacement of the cool and warm ISM in the galaxy, due to the pressure of the relativistic particles.

The left-hand panel of Fig. 14 compares the morphology of the lower frequency radio emission to that of the high-frequency radio emission and the X-ray gas. At lower frequencies the orientation of the radio extension is rotated clockwise with respect to the high-frequency emission. The rotation is in the same sense as the Hα filament (see Fig. 14, right-hand panel) and the 614 MHz contours (green contours) show a spur of emission which follows the filament in the north-easterly direction.

6 DISCUSSION

A distinguishing feature of many BCGs in cool-core clusters, where heating is required to prevent catastrophic cooling of the hot gas,

Table 3. Results from the multitemperature fits to regions 1–4 in Fig. 12.

Region	Model	C stat	kT (keV)	Norm (cm^{-5})	Si	S	Fe	Ni
					Abundances in solar units			
Region1	VAPEC	336.94/315	$1.29^{0.02}_{-0.02}$	$0.000\,88^{6.7e-05}_{-6.6e-05}$	$0.58^{0.10}_{-0.09}$	$0.65^{0.18}_{-0.16}$	$0.27^{0.05}_{-0.05}$	$0.62^{0.44}_{-0.41}$
		1.070						
	2 × VAPEC	316.743/313	$0.36^{0.04}_{-0.08}$	$0.000\,11^{5.9e-05}_{-2.1e-05}$	$1.11^{0.35}_{-0.29}$	$1.04^{0.37}_{-0.31}$	$0.40^{0.11}_{-0.09}$	$1.45^{0.82}_{-0.77}$
		1.011	$1.50^{0.08}_{-0.08}$	$0.000\,57^{0.000\,11}_{-8.6e-05}$				
Region2	VAPEC	229.293/251	$1.32^{0.03}_{-0.04}$	$0.000\,29^{2.2e-05}_{-3.6e-05}$	$0.68^{0.21}_{-0.16}$	$0.86^{0.37}_{-0.29}$	$0.33^{0.08}_{-0.087}$	$0.86^{0.95}_{-0.79}$
		0.914						
	2 × VAPEC	220.801/249	$1.5^{0.16}_{-0.12}$	$0.000\,21^{5e-05}_{-5.8e-05}$	$1^{0.58}_{-0.29}$	$1.1^{0.69}_{-0.41}$	$0.51^{0.27}_{-0.16}$	$0.99^{1.4}_{-0.99}$
		0.887	$0.81^{0.22}_{-0.17}$	$1.9e-05^{2.4e-05}_{-8.1e-06}$				
Region3	VAPEC	335.605/340	$1.6^{0.045}_{-0.054}$	$0.000\,55^{3.4e-05}_{-3.3e-05}$	$1^{0.18}_{-0.17}$	$0.73^{0.27}_{-0.25}$	$0.48^{0.08}_{-0.086}$	$1.2^{0.7}_{-0.66}$
		0.987						
	2 × VAPEC	332.939/338	17^{-17}_{-17}	$1.8e-05^{0.000\,49}_{-1.8e-05}$	$1.2^{0.31}_{-0.24}$	$0.85^{0.36}_{-0.29}$	$0.5^{0.12}_{-0.11}$	$1.8^{1.3}_{-0.95}$
		0.985	$1.6^{0.063}_{-0.33}$	$0.000\,49^{7.3e-05}_{-0.000\,49}$				
Region4	VAPEC	447.967/408	$1.99^{0.23}_{-0.25}$	$0.000\,4566^{0.000\,0605}_{-0.000\,0687}$	$0.42^{0.32}_{-0.29}$	$0.43^{0.51}_{-0.43}$	$0.35^{0.16}_{-0.13}$	$0.62^{1.10}_{-0.62}$
		1.09						
	2 × VAPEC	447.966/406	$0.08^{-0.08}_{-0.08}$	$0.00^{-0.00}_{0.822}$	$0.42^{0.32}_{-0.29}$	$0.44^{0.50}_{-0.44}$	$0.34^{0.17}_{-0.13}$	$0.63^{1.09}_{-0.63}$
		1.10	$1.98^{0.23}_{-0.24}$	$0.000\,45^{0.000\,062}_{-0.000\,069}$				

is that they harbour intricate extended systems of low-ionization optically emitting gas. A significant body of work has studied the origin of these filaments and their relationship with star formation, AGN feedback and gas in other phases. The BGG IC 4374 in Abell 3581 is one such system where it is clear that the structures in the hot, cool and cold dusty gas are intimately related and are connected with the presence of the radio lobes.

IC 4374 exhibits prominent dust lanes running north and south through the galaxy nucleus. Both these dust lanes have extensions to the east which trace the ionized gas filaments (Fig. 3). A young star cluster is observed in the northern wedge shaped dust lane but no other evidence for star formation, notably none in the filament system, is observed.

Scaling from our $E(B-V)$ map (Fig. 4) of relative intrinsic dust extinction and assuming a hydrogen column density of $N_{\rm H} = 5.8 \times 10^{21} \times E(B-V)$ and the Galactic gas to dust ratio, ∼100, allows us to estimate the dust mass in the galaxy as $10^6\,M_\odot$ with $\sim10^5\,M_\odot$ in the south-east filament.

The morphology of the Hα+[N II] emission is matched very well by the coolest and highest density regions of the X-ray gas (Fig. 8). The optical filaments engulf the inner bubbles and are coincident with the easterly extending dust lanes. The smooth velocity gradients of the ionized gas suggest that the filaments extending around the bubbles are continuous.

The south-west filament leads to an outer bubble. Cool, low-metallicity X-ray gas also extends from the centre of the cluster in the direction of this bubble and there is a discontinuity in the properties of the X-ray gas at a radius corresponding to the inner edge of the bubble. The lower frequency radio emission is rotated clockwise with respect to the high-frequency emission and is aligned along the axis of the outer, not the inner, bubble (see Fig. 14).

A spiral of high-metallicity, low-temperature, low-entropy X-ray gas, with a cold front at its outer edge, is observed to trail from the cool core. In the following sections, we draw on these observations to attempt to answer questions pertinent to the nature of the heating and cooling cycle in this system.

6.1 Origin of filaments and dust lanes

The filaments in Abell 3581 exhibit point symmetry but are not radial, varying direction as they extend out of the galaxy. We cannot comment on the extent of the directional change as this depends on the projection angle. The velocity structure of the filaments is smooth, consistent with the cool gas being pushed aside due to the expansion of the inner radio bubbles and, importantly, both the eastern filament extensions (the blueshifted and redshifted sides of the filament) are accompanied by thin threads of dust.

Initial dust grain formation requires high densities and low enough temperatures to permit the condensation of silicates and graphites; it therefore cannot form straight out of a dust-free ICM. However, Draine (2003) makes the point that our current knowledge of grain destruction time-scales and observed element depletions in the gas-phase highlight that much of the subsequent dust growth must happen through interstellar processing. Dust and polycylic aromatic hydrocarbon features have both been found in the extended ionized gas filaments of other BCGs (e.g. Sparks, Macchetto & Golombek 1989; Johnstone et al. 2007; Donahue et al. 2011).

The rim of the inner bubble, east of the nucleus, is laced with emission from ionized gas apparently encasing the bubble, implying the hot gas inflating the bubble is sweeping aside the cooler ionized gas. The south-west filament ends at the discontinuity in surface brightness, temperature and metallicity delineating the inner edge of the outer bubble indicating that this filament may have been dragged up beneath the outer bubble. The correlation observed between the cool gas and dust filaments, X-ray cavities and the radio emission and the symmetry of the two filament extensions is hard to reconcile within the framework of filaments cooling from the hot ICM in situ or being the result of a galaxy merger.

It is therefore tempting to advocate that this outer bubble and another in the opposite direction are responsible for the displacement of cool gas seeding the extended filaments and an interaction between the cool uplifted material and the hot ICM is responsible for the cooler X-ray gas (e.g. see discussion in Werner et al. 2013)

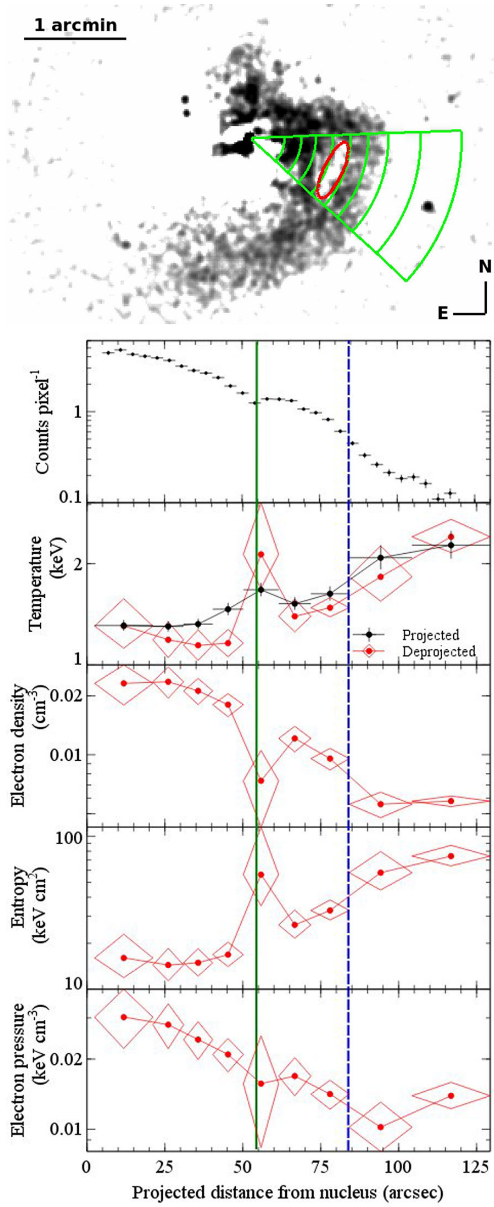

Figure 13. Temperature, density and pressure profiles in a sector chosen to include the cavity and cold front. The widths of the annuli are determined by requiring a minimum of 3000 counts per annuli and are shown in the image above. The green solid line on the figure indicates the radius of the centre of the outer cavity while the blue dashed line indicates the radius of the cold front.

However, we note that by eye, we do not observe a second outer bubble. The X-ray surface brightness is not symmetrical about the nucleus; the surface brightness drops more sharply in the north-east of Abell 3581 than in the south-west (Fig. 15) which might inhibit our view of a second outer bubble.

Crudely, we test the hypothesis that the corresponding north-eastern outer bubble is not observed due to the low surface brightness by examining the significance of a similar outer bubble (same size/shape), reflected through the nucleus of Abell 3581.

To quantify the significance of a bubble, we compare the counts in the 'bubble region' to regions on either side of the bubble and with the same shape and radius. For our detected outer bubble, we find an ~10 per cent decrement in counts (~3010 counts compared with ~3390 counts in the undisturbed regions) corresponding to an ~6σ deficit. If we assume a similar size and shape bubble with point symmetry through the nucleus, we find an ~5 per cent decrement (~2119 and ~2196 counts) corresponding to ~1.5σ. A 10 per cent deficit in counts in this low surface brightness region, similar to the deficit seen in the outer bubble, would still only amount to a 3σ detection of a broad bubble and is probably not easily observed by eye. We may not expect to see a bubble with the same size and shape and at the same radius. The surface brightness drop indicates a lower gas density. We might expect a bubble to be larger in size in a less dense medium further decreasing the likelihood of observing it. We cannot rule out the possibility of another outer bubble being responsible for the gas uplift of the filaments towards the north-east. We also note that a depression in the surface brightness profile is observed at ~40 arcsec from the nucleus towards the north-east direction (see Fig. 15) which lends supporting evidence for another outer bubble.

The emission lines in the central regions of the galaxy have very large measured velocity dispersions particularly towards the eastern inner cavity. Our data are unable to constrain two or more velocity components to the line emission but it is likely that multiple velocity components contribute to the broad velocity features observed. Farage et al. (2012) suggest that the broad blueshifted feature is indicative of an inflow, perhaps responsible for feeding the AGN. We suggest that the line-of-sight velocities, blueshifted in one direction and redshifted in the other, are consistent with the expansion of a radio bubble pushing aside the cool gas as it expands. This cool gas may have existed in an extended structure due to outflows from previous bubbles. The action of the current inner radio bubbles is to sweep aside the cool gas and to expand in the direction of least resistance. The coincidence of both the north-east and south-east filaments with filamentary dust lanes supports the idea that the gas is being lifted/pushed away from the centre of the galaxy.

High spatial resolution observations of the cold gas, for example with Atacama Large Millimeter/submillimeter Array (ALMA) or Spectrograph for INtegral Field Observations in the Near Infrared (SINFONI) IFU, would shed light on the presence of an inflow or outflow in the nucleus.

6.1.1 *Origin of the gas central to the galaxy*

Having argued that the gas in the filaments originates in gas uplifted from the central galaxy, the question then becomes, did the cool and cold gas in the galaxy originate from the cooling hot ICM or through stellar mass loss of the BCG or its principal merger constituents? This is a complicated question and the answer is probably both, but whether a dominant mechanism is at play is not known.

Abell 3581 has a total Hα flux of 6.9×10^{-14} erg cm^{-2} s^{-1}; this translates to a mass, $M_{\mathrm{H}^+} = 2.6 \times 10^6\,\mathrm{M}_{\odot}$ assuming $n_e \sim 100\,\mathrm{cm}^{-3}$ and that the effective recombination coefficient of Hα is $\alpha^{\mathrm{eff}} = 1.17 \times 10^{-13}\,\mathrm{cm}^3\,\mathrm{s}^{-1}$ (Osterbrock & Ferland 2006). CO(2−1) emission has also been detected in the central galaxy. The CO luminosity is $2.35 \times 10^7\,\mathrm{K\,km\,s^{-1}\,pc^2}$; assuming the standard conversion factor ($M_{\mathrm{gas}}/L'_{\mathrm{CO}} = 4.6\,\mathrm{M}_{\odot}(\mathrm{K\,km\,s^{-1}\,pc^2})^{-1}$), the mass of molecular gas estimated from the IRAM observations of the nucleus of Abell 3581 is $\sim 1 \times 10^8\,\mathrm{M}_{\odot}$. The observable dust mass, estimated from our $E(B - V)$ map, is $10^6\,\mathrm{M}_{\odot}$.

Sanders et al. (2010) find a mass deposition rate of about $0.4\,\mathrm{M}_{\odot}\,\mathrm{yr}^{-1}$ in the central regions of Abell 3581 and a cooling time for this gas of $\sim 10^8$ yr. The coolest X-ray gas is morphologically similar to the optical filaments. If these filaments are seeded by

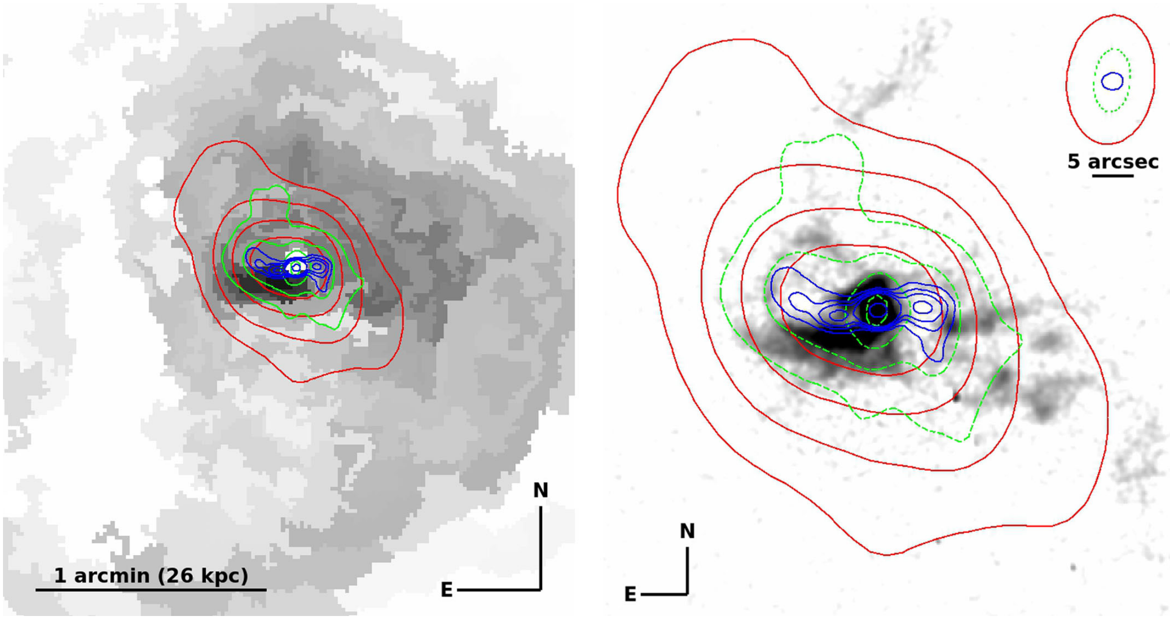

Figure 14. Left: X-ray temperature map overlaid with contours of radio emission. Red contours are from 244 MHz GMRT emission, green contours from 614 MHz GMRT emission and the central blue contours are from *L*-band JVLA radio emission. Low-temperature gas (darker colours, see Figs 8 and 9) is observed at the centre of the system and stretches east and west from the nucleus towards the bubbles. Right: the same radio contours overlaid on the SOAR net Hα image. The beam sizes are shown in the top-right corner of the image.

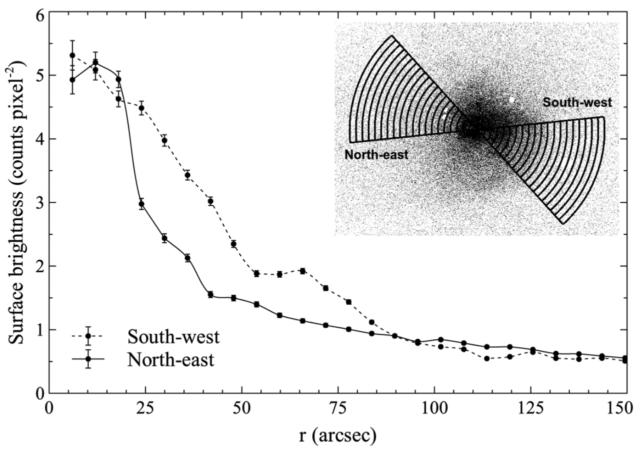

Figure 15. X-ray surface brightness profile towards the outer X-ray cavity (south-west) and in a direction reflected through the nucleus (north-east). The X-ray emission is not radially symmetric; in the north-east direction the cluster surface brightness drops much more sharply than towards the south-west. The outer cavity in the south-west is at a distance of ∼55 arcsec.

being dredged up out of the galaxy by the bubbles, then the outer filaments are approximately the age of the outer bubble, $\sim 5 \times 10^7$ yr. In this time, making the extreme assumptions that 100 per cent of the gas cools and that the mass deposition rate has not changed, the X-ray contribution to the filaments could be up to 2×10^7 M$_\odot$, easily accounting for the mass of cool gas in the filaments but nearly an order of magnitude shy of the expected cold gas content of the central galaxy. If the filaments are currently growing in mass, some dusty gas must have existed to seed the filaments in the first place. It should be noted that we do not yet know the exact morphology of the cold molecular gas in Abell 3581; however, cold molecular gas has been found coincident with extended ionized filaments in many systems (e.g. Hatch et al. 2005; Johnstone et al. 2007; Oonk et al. 2010; Donahue et al. 2011; Mittal et al. 2011; Salomé et al. 2011; Werner et al. 2013; Werner et al., in preparation).

The SFRs given by *WISE* infrared and by *GALEX* near- and far-ultraviolet emission are ∼0.21, 0.3 and 0.1 M$_\odot$ yr^{-1}, respectively, close to the current mass deposition rate measured from the cool X-ray gas. However, the morphologies of these two components are very different. The star formation is centred on the nucleus and a single bright young star cluster, and is roughly symmetrical, while the cool X-ray gas is asymmetrically distributed and much of it is associated with the filaments.

Fig. 16 shows that in the lifetime of a BGG, a significant fraction of its stellar mass will be returned to the ISM and its various gas phases. The evolved stellar population is currently contributing ∼1 M$_\odot$ yr^{-1} (estimate for a 10^{11} M$_\odot$ galaxy). This is comparable to the cooling rate of the hot gas and the SFR, and as such the stellar mass loss may be an important contributor to the current cool and cold gas being generated in the galaxy.

We are unable to conclude whether one mechanism dominates over the other; both stellar mass loss and the cooling gas may be providing similar cool gas quantities currently. The stellar mass loss in total, over the lifetime of the population, must be significant; however, how much of the mass is maintained in the cool/cold gas phases is not known. How X-ray mass deposition rates and the heating of the X-ray gas have varied with time is also not known. The more abundant cool and cold gas in BCGs within galaxy clusters with cool cores, as opposed to non-cool-core galaxy clusters, suggests that the high-pressure environment must play a role.

6.2 Filament excitation

Clues about the filament excitation mechanisms can be gleaned through Fig. 7. Near the nucleus there is both a gradient in the [N II] λ6583/Hα emission-line ratio, decreasing rapidly from the nucleus (dropping by a factor of 2 within 5 arcsec), and a gradient

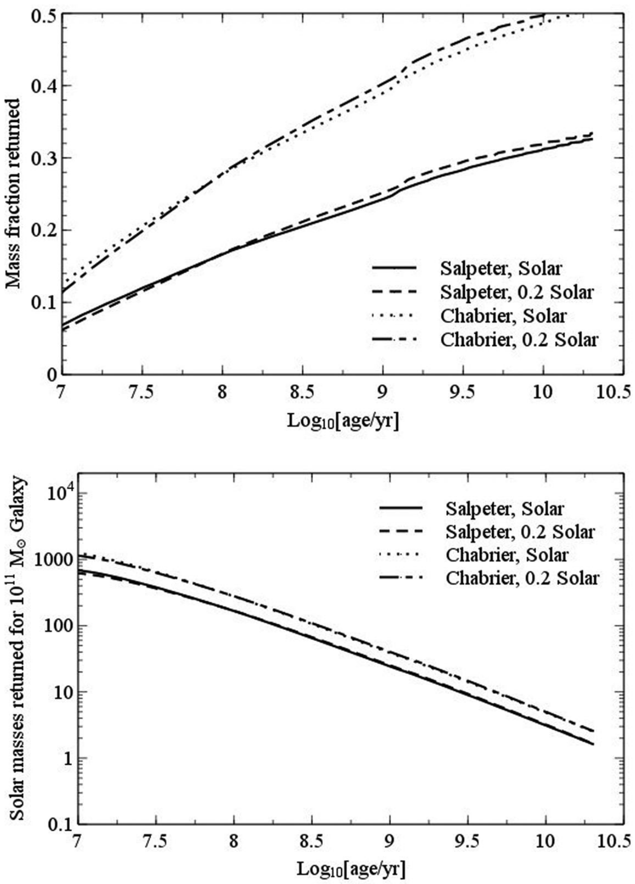

Figure 16. The time evolution of mass-loss for a simple stellar population (SSP) which has been born at time $t = 0$ using the models of BC03 (Bruzual & Charlot 2003). The fraction of the stellar mass returned is very IMF dependent but only mildly dependent on metallicity.

from the inside to the outside of the nearby filaments (dropping by a factor of ∼1.5 across the filament width). Farther out in the filaments, the ratio shows less variation.

At a fixed metallicity and density the [N II] λ6583/Hα ratio is essentially an indicator of the amount of heating in the gas per hydrogen ionization. However, collisional excitation may be more efficient at higher densities, and increases in the nitrogen abundance in the gas will increase the [N II] λ6583/Hα ratio. The observed gradient could be indicative of an extra heating mechanism, such as photoionization by the AGN or a weak shock or interaction driven by the AGN outflow, or a metallicity or density gradient in the gas.

As we suspect that the gas originates in the galaxy and has been dragged out and pushed aside by the inflating radio bubbles, strong metallicity gradients over small regions of the filament are unlikely. [O III] λ5007 is typically weak in the extended filaments in BCGs. Indeed, it is too weak to observe in our outer filaments, but is strong in the filament sections close to the nucleus and where the velocity widths of the lines are large. We observe a strong gradient (> factor 3 increase) in [O III] λ5007 emission from the 'inside' of the southern filament, adjacent to the radio bubble, to the 'outside' and an accompanying strong gradient in the ratio of [O III] λ5007 to Hα emission. Unfortunately the wavelength range of our spectrum does not include [O III] λ4363 emission so we are unable to estimate the kinetic temperature variations across the filament.

[S II] λ6716/[S II] λ6731 is a diagnostic of the electron density. Ratios >1.3 are typical of the low-density limit (<100 cm^{-3}) while the high-density limit is characterized by ratios of <0.5 (>1000 cm^{-3}). Typically, extended filaments have been found to lie in the low-density limit (e.g. Hatch et al. 2006) and this is consistent with our observed values.

We observe emission lines of [N I] λ5199 in the filaments. This emission is usually weak in gas with a well-defined kinetic temperature. This is due to the excitation potential being similar in magnitude to the ionization potential of H^0. There is often little N^0 present in warm gas and so little [N I] λ5199 emission (see Ferland et al. 2009, 2012 for further discussion of [N I] λ5199 excitation mechanisms). A mechanism which produces supra-thermal particles in the gas and can create some level of ionization even within cold gas, gas which is multiphase on a microscopic level, would be successful at reproducing these line ratios (Ferland et al. 2009). Such a mechanism, provided by the surrounding hot ISM/ICM, has been suggested by Ferland et al. (2008, 2009) and Fabian et al. (2011). Additionally, Churazov, Ruszkowski & Schekochihin (2013) have suggested non-thermal particles created in situ in the magnetically supported filaments may contribute to the emission-line spectra.

The variation in the emission-line ratios shown in Table 2 highlights the complicated nature of the filament excitation mechanisms in regions which are not isolated, such as those close to the nucleus or close to inflating radio bubbles. Clearly, several excitation mechanisms are at play in the inner regions of this filament system and disentangling them is not trivial. It may not be informative to study the emission-line ratios in large regions of the centres of these systems; choosing specific 'clean' regions where one mechanism dominates is preferable.

6.3 Jet precession/bulk motions of ICM

The current bubble axis in IC 4347 has east–west point symmetry through the nucleus. However, the outer bubble appears twisted ∼20° south from the westerly direction (in projection); a twist which is also reflected in the trailing Hα filaments and the high-to-low frequency radio emission. Lower frequency radio emission probes less energetic plasmas, therefore older bubbles. The effect of bubble wobbling is unlikely to account for the change in the orientation of the radio emission axis as this need not affect both the bubbles in the same way.

Bubble rise directions do not appear to be consistent; some systems exhibit directional changes between outbursts but, for the most part, maintain point symmetry (e.g. NGC 1275; Fabian 2012). Dunn, Fabian & Sanders (2006) suggested a precessing jet may be responsible for the directional change in the three most recent outbursts of NGC 1275. A motivating feature for this model is that the filaments are largely radial. The bubble direction may also have changed due to turbulence or gas motions within the nuclear region and subsequently risen in the 'easiest' direction – that of the lowest pressure – however, it is not obvious that this would lead to bubbles with approximate point symmetry. If the precession model is an explanation for the Abell 3581 bubbles, assuming that the bubbles are rising in the plane of the sky, the measured angle between the inner and outer bubbles in Abell 3581 gives a precession rate of 6° per 10^7 yr.

NGC 5044 exhibits bubbles which are rising in various directions in the cluster (David et al. 2009, 2011). The authors suggest that the nearly isotropic distribution of the bubbles is a result of the group 'weather' from AGN-driven turbulence generated by many small outbursts or from the sloshing of NGC 5044 with respect to the group potential (e.g. see simulations of Brüggen, Ruszkowski & Hallman 2005; Heinz et al. 2006). Finally, a beautiful example of linearly rising bubbles is shown by Randall et al. (2011) in their X-ray images of NGC 5813.

Some clues as to the directional change in Abell 3581 are given by observations of the same twist in the optical and radio emission and the large-scale spiral structure observed in the hot X-ray gas beyond the outer bubble (Fig. 9). Fig. 13 shows evidence for a jump in temperature, a density dip and approximate pressure equilibrium coincident with the outer edge of the spiral, consistent with a cold front.

Similar structures have been observed in many X-ray images of cluster cool cores (e.g. Churazov et al. 2000; Fabian et al. 2000; Markevitch, Vikhlinin & Mazzotta 2001; Mazzotta et al. 2001; Churazov et al. 2003; Dupke & White 2003; Markevitch et al. 2003; Mazzotta, Edge & Markevitch 2003; Clarke, Blanton & Sarazin 2004; Sanders, Fabian & Dunn 2005; Sanders et al. 2009). In relaxed clusters, the current paradigm is that these cold fronts are caused by gas sloshing within the cluster cool core. The sloshing may be a result of a disturbance caused by the in-fall or fly-by of a subcluster or alternatively a disturbance associated with energy injection into the ICM by the AGN (for a review see Markevitch & Vikhlinin 2007).

Jones et al. (2002), Baldi et al. (2009) and David et al. (2009) have found similar spiral features in NGC 4636 and NGC 5044, respectively, with the distinguishing feature that these spirals appear to have two arms. Simulations of cluster sloshing have thus far produced one-armed spirals. In NGC 5044, David et al. (2009) suggests the group weather has been responsible for perturbing the buoyant bubbles rise paths causing them to drag cooler, metal-rich material out of the galaxy in two spirals; one emanating from each jet. The 'weather' is perhaps still generated by bulk sloshing motions but the cooler gas is now dredged up from the nucleus rather than cooling from the core. NGC 4636 differs in that its spiral arms are hotter, not colder than the surrounding medium suggesting these are the result of shocks driven into the ICM due to the inflation of the bubbles.

In Abell 3581, the X-ray data appear to favour a single spiral structure. The slow rotation in the radio emission and the directional change along the filaments indicates that the rise direction differences are not due to jet precession and that some other process changed the bubbles direction after it had left the nucleus. This is unlikely to be simply the path of least pressure as there is a rotational symmetry to the directional change in the filaments. The projected twist direction is clockwise and is the same direction in which the spiral unravels. The stirring of the ICM from some previous disturbance could be responsible for this.

6.4 Cooling and heating

Active AGN heating is ongoing in the core of Abell 3581. Bubbles are being produced and rising into the ICM dragging with them multiphase filaments. The cool and cold gas and dust phases are presumably interacting with the hot surrounding medium resulting in the cool, low-volume filling, X-ray emission.

The X-ray luminosity in the core (at a radius of the inner bubbles) is extremely well matched by the powers of the inner bubbles, $L_X \sim 2.1 \times 10^{42}$ erg s^{-1} and $P_{cav} \sim 2.2 \times 10^{42}$ erg s^{-1}, respectively. However, assuming that the outer bubble to the west of the nucleus is part of a pair, the outer and inner cavity powers, $P_{cav} \sim 3.1 \times 10^{42}$ erg s^{-1}, are more than a factor of 2 lower than the X-ray luminosity in a circular region with a radius of the projected distance of the outer cavity ($L_X \sim 7.8 \times 10^{42}$ erg s^{-1}) and significantly smaller than the X-ray luminosity within the 'cooling radius' (assumed to be where $t_{cool} < 7.7$ Gyr, $L_X \sim 1.1 \times 10^{43}$ erg s^{-1}). If the bays observed to the south and east are additional bubbles, the total cavity heating within this region may be significantly larger.

The high-metallicity, low-entropy spiral of gas emanating from the core is indicative of ongoing stripping of the X-ray cool core. This stripping is distributing low-entropy material over a larger radius in the cluster in a manner reminiscent of that observed in the much more massive Ophiuchus Cluster (Million et al. 2010). The mass of the cool core inside a radius of 30 arcsec (∼13 kpc) is $\sim 10^{10}$ M$_{\odot}$. Taking the density from Fig. 11 and a conservative cylindrical volume representative of the brightest part of the spiral, with dimensions 2 arcmin in length by 10 arcsec in radius, we estimate the mass of the stripped spiral arm to be $\sim 8 \times 10^8$ M$_{\odot}$ (making the assumption of 100 per cent filling factor) or ∼8 per cent of the current cool core. Assuming the sound speed of the gas ∼400 km s^{-1}, the time taken for gas to travel the 2 arcmin from the core to the end of the cylindrical volume in which we have measured the gas mass is $\sim 1.3 \times 10^8$ yr. Thus, stripping of this rate could in principle destroy the cool core in 1–2 Gyr, although ongoing cooling (the cooling time in this region is comparable, $\sim 10^9$ yr) will also replenish it.

7 CONCLUSIONS

Abell 3581 has a rich multiphase phenomenon not common in X-ray groups. There is evidence for multiple 'radio-mode' outbursts of activity from the central AGN and it is clear that the resulting bubbles are interacting with the cold, cool and hot gas in the system. We summarize our main conclusions below:

(i) The BGG, IC 4373, exhibits bright cool ionized gas filaments extending over 30 arcsec (∼13 kpc) from the nucleus. These filaments are coincident with dust and soft X-ray emission. The filaments engulf the inner east–west bubbles and then change direction extending towards older cavities in the south-west and north-east.

(ii) Based on the morphology of the X-ray cavities, radio emission and cool gas filaments and on the filament kinematics, we suggest that gas uplifted, by the radio bubbles, from the centre of the galaxy is responsible for the extended, filamentary nature of the ionized gas nebulosity.

(iii) The conclusion that the filamentary gas originated from the uplift of material from the core of the galaxy rather than the filaments condensing directly from the hot ICM is supported by the presence of the dust in the filaments which is likely seeded by stellar mass loss in the centre of the galaxy.

(iv) The line emission close to the nucleus and coincident with the direction of the jet has very high velocities indicative of an outflow.

(v) The BCG has an SFR of about 0.2–0.3 M$_{\odot}$ yr^{-1}, as measured by *WISE* and *GALEX*. A young blue star cluster is also revealed in the *HST* data. The SFR is comparable to the X-ray mass deposition rate (0.4 M$_{\odot}$ yr^{-1}) from the *XMM* Reflection Grating Spectrometer spectral analysis (Sanders et al. 2010).

(vi) Farther out on the filament system, the emission-line ratios are similar to those seen in the extended filaments of other BCGs exhibiting characteristically low [O III] λ5007 emission and relatively strong [N I] λ5199 emission. It is probable that many excitation mechanisms are occurring in the 'messy' inner regions of the galaxy while the outer 'cleaner' regions are consistent with an excitation mechanism which produces some level of ionization even in cold gas, such as collisions with supra-thermal particles from the hot ISM/ICM.

(vii) The presence of the cold front and the directional change of the bubbles and filaments indicates that the group weather, driven by sloshing, may be controlling the rise direction of the bubbles.

(viii) The spiral cold front exhibits higher metallicities and lower entropy than the surrounding gas and is similar in its X-ray properties to the cool core. The spiral could be material, stripped from the core due to sloshing motions.

ACKNOWLEDGEMENTS

Support for this work was provided by NASA through award number 1428053 issued by JPL/Caltech. REAC acknowledges a scholarship from the Cambridge Philosophical Society and a Royal Astronomical Society grant. MS is supported by the NASA grants GO1-12103A, NNH12CG03C and HST-GO-12373. TEC was supported in part for this work by the National Aeronautics and Space Administration, through Chandra Award Number GO1-12159Z. Basic research in radio astronomy at the Naval Research Laboratory is supported by 6.1 Base funding. SG acknowledges the support of NASA through Einstein Postdoctoral Fellowship PF0-110071 awarded by the Chandra X-ray Center (CXC), which is operated by SAO. SWA acknowledges support from the US Department of Energy under contract number DE-AC02-76SF00515. PEJN was supported by NASA contract NAS8-03060. CLS was supported in part by NASA Chandra Grant G01-12169X. REAC would also like to thank Anja von der Linden and Adam Mantz for interesting and enlightening discussions. This research has made use of the NASA/IPAC Extragalactic Database (NED) which is operated by the Jet Propulsion Laboratory, California Institute of Technology, under contract with the National Aeronautics and Space Administration.

REFERENCES

Anders E., Grevesse N., 1989, Geochim. Cosmochim. Acta, 53, 197
Baldi A., Forman W., Jones C., Kraft R., Nulsen P., Churazov E., David L., Giacintucci S., 2009, ApJ, 707, 1034
Bîrzan L., Rafferty D. A., McNamara B. R., Wise M. W., Nulsen P. E. J., 2004, ApJ, 607, 800
Blanton E. L., Sarazin C. L., McNamara B. R., Wise M. W., 2001, ApJ, 558, L15
Brüggen M., Ruszkowski M., Hallman E., 2005, ApJ, 630, 740
Bruzual G., Charlot S., 2003, MNRAS, 344, 1000
Canning R. E. A., Fabian A. C., Johnstone R. M., Sanders J. S., Crawford C. S., Ferland G. J., Hatch N. A., 2011, MNRAS, 417, 3080
Cardelli J. A., Clayton G. C., Mathis J. S., 1989, ApJ, 345, 245
Cavagnolo K. W., McNamara B. R., Nulsen P. E. J., Carilli C. L., Jones C., Bîrzan L., 2010, ApJ, 720, 1066
Churazov E., Forman W., Jones C., Böhringer H., 2000, A&A, 356, 788
Churazov E., Forman W., Jones C., Böhringer H., 2003, ApJ, 590, 225
Churazov E., Ruszkowski M., Schekochihin A., 2013, preprint (arXiv:1304.3168)
Clarke T. E., Blanton E. L., Sarazin C. L., 2004, ApJ, 616, 178
Conselice C. J., Gallagher J. S., III, Wyse R. F. G., 2001, AJ, 122, 2281
Cornwell T. J., Holdaway M. A., Uson J. M., 1993, A&A, 271, 697
Cowie L. L., Hu E. M., Jenkins E. B., York D. G., 1983, ApJ, 272, 29
Crawford C. S., Fabian A. C., 1992, MNRAS, 259, 265
Crawford C. S., Allen S. W., Ebeling H., Edge A. C., Fabian A. C., 1999, MNRAS, 306, 857
Danziger I. J., Focardi P., 1988 in Fabian A. C., ed., NATO ASIC Proc. 229: Cooling Flows in Clusters and Galaxies. Kluwer, Dordrecht, p. 133
David L. P., Jones C., Forman W., Nulsen P., Vrtilek J., O'Sullivan E., Giacintucci S., Raychaudhury S., 2009, ApJ, 705, 624
David L. P. et al., 2011, ApJ, 728, 162
De Grandi S., Molendi S., 2001, ApJ, 551, 153
Diehl S., Li H., Fryer C. L., Rafferty D., 2008, ApJ, 687, 173
Donahue M., Mack J., Voit G. M., Sparks W., Elston R., Maloney P. R., 2000, ApJ, 545, 670
Donahue M., de Messières G. E., O'Connell R. W., Voit G. M., Hoffer A., McNamara B. R., Nulsen P. E. J., 2011, ApJ, 732, 40
Draine B. T., 2003, ARA&A, 41, 241
Dunn R. J. H., Fabian A. C., Taylor G. B., 2005, MNRAS, 364, 1343
Dunn R. J. H., Fabian A. C., Sanders J. S., 2006, MNRAS, 366, 758
Dupke R., White R. E., III, 2003, ApJ, 583, L13
Edge A. C., 2001, MNRAS, 328, 762
Edge A. C. et al., 2010, A&A, 518, L47
Edwards L. O. V., Robert C., Mollá M., McGee S. L., 2009, MNRAS, 396, 1953
Fabian A. C., 1994, ARA&A, 32, 277
Fabian A. C., 2012, ARA&A, 50, 455
Fabian A. C. et al., 2000, MNRAS, 318, L65
Fabian A. C., Sanders J. S., Ettori S., Taylor G. B., Allen S. W., Crawford C. S., Iwasawa K., Johnstone R. M., 2001, MNRAS, 321, L33
Fabian A. C. et al., 2011, MNRAS, 418, 2154
Farage C. L., McGregor P. J., Dopita M. A., Bicknell G. V., 2010, ApJ, 724, 267
Farage C. L., McGregor P. J., Dopita M. A., 2012, ApJ, 747, 28
Ferland G. J., Fabian A. C., Hatch N. A., Johnstone R. M., Porter R. L., van Hoof P. A. M., Williams R. J. R., 2008, MNRAS, 386, L72
Ferland G. J., Fabian A. C., Hatch N. A., Johnstone R. M., Porter R. L., van Hoof P. A. M., Williams R. J. R., 2009, MNRAS, 392, 1475
Ferland G. J., Henney W. J., O'Dell C. R., Porter R. L., van Hoof P. A. M., Williams R. J. R., 2012, ApJ, 757, 79
Fruscione A. et al., 2006 in Silva D. R., Doxsey R. E., eds, Proc. SPIE Conf. Ser. Vol. 6270, Observatory Operations: Strategies, Processes, and Systems. SPIE, Bellingham, p. 62701
Gastaldello F., Molendi S., 2004, ApJ, 600, 670
Giacintucci S. et al., 2011, ApJ, 732, 95
Gitti M., O'Sullivan E., Giacintucci S., David L. P., Vrtilek J., Raychaudhury S., Nulsen P. E. J., 2010, ApJ, 714, 758
Gu J., Xu H., Gu L., An T., Wang Y., Zhang Z., Wu X.-P., 2007, ApJ, 659, 275
Hatch N. A., Crawford C. S., Fabian A. C., Johnstone R. M., 2005, MNRAS, 358, 765
Hatch N. A., Crawford C. S., Johnstone R. M., Fabian A. C., 2006, MNRAS, 367, 433
Hatch N. A., Crawford C. S., Fabian A. C., 2007, MNRAS, 380, 33
Heckman T. M., Baum S. A., van Breugel W. J. M., McCarthy P., 1989, ApJ, 338, 48
Heinz S., Brüggen M., Young A., Levesque E., 2006, MNRAS, 373, L65
Hu E. M., Cowie L. L., Kaaret P., Jenkins E. B., York D. G., Roesler F. L., 1983, ApJ, 275, L27
Jaffe W., Bremer M. N., 1997, MNRAS, 284, L1
Johnstone R. M., Fabian A. C., Nulsen P. E. J., 1987, MNRAS, 224, 75
Johnstone R. M., Fabian A. C., Morris R. G., Taylor G. B., 2005, MNRAS, 356, 237
Johnstone R. M., Hatch N. A., Ferland G. J., Fabian A. C., Crawford C. S., Wilman R. J., 2007, MNRAS, 382, 1246
Jones C., Forman W., Vikhlinin A., Markevitch M., David L., Warmflash A., Murray S., Nulsen P. E. J., 2002, ApJ, 567, L115
Kalberla P. M. W., Burton W. B., Hartmann D., Arnal E. M., Bajaja E., Morras R., Pöppel W. G. L., 2005, A&A, 440, 775
Kennicutt R. C., Jr, 1998, ARA&A, 36, 189
Kotulla R., Fritze U., Weilbacher P., Anders P., 2009, MNRAS, 396, 462
Kroupa P., 2002, Sci, 295, 82
Le Fèvre O. et al., 2003 in Iye M., Moorwood A. F. M., eds, Proc. SPIE Conf. Ser. Vol. 4841, Instrument Design and Performance for Optical/Infrared Ground-based Telescopes. SPIE, Bellingham, p. 1670
Lynds R., 1970, ApJ, 159, L151

McNamara B. R., Nulsen P. E. J., 2007, ARA&A, 45, 117
McNamara B. R. et al., 2000, ApJ, 534, L135
Markevitch M., Vikhlinin A., 2007, Phys. Rep., 443, 1
Markevitch M., Vikhlinin A., Mazzotta P., 2001, ApJ, 562, L153
Markevitch M. et al., 2003, ApJ, 586, L19
Markwardt C. B., 2009 in Bohlender D. A., Durand D., Dowler P., eds, ASP Conf. Ser. Vol. 411, Astronomical Data Analysis Software and Systems XVIII. Astron. Soc. Pac., San Francisco, p. 251
Mathews W. G., Buote D. A., Brighenti F., 2001, ApJ, 550, L31
Mazzotta P., Markevitch M., Vikhlinin A., Forman W. R., David L. P., van Speybroeck L., 2001, ApJ, 555, 205
Mazzotta P., Edge A. C., Markevitch M., 2003, ApJ, 596, 190
Million E. T., Allen S. W., Werner N., Taylor G. B., 2010, MNRAS, 405, 1624
Mittal R. et al., 2011, MNRAS, 418, 2386
Moré J. J., 1978, The Levenberg-Marquardt Algorithm: Implementation and Theory. Springer, Berlin
Oonk J. B. R., Jaffe W., Bremer M. N., van Weeren R. J., 2010, MNRAS, 405, 898
Osterbrock D. E., Ferland G. J., 2006, Astrophysics of Gaseous Nebulae and Active Galactic Nuclei. University Science Books, Mill Valley, CA
O'Sullivan E., Giacintucci S., David L. P., Gitti M., Vrtilek J. M., Raychaudhury S., Ponman T. J., 2011, ApJ, 735, 11
Perley R. A., Chandler C. J., Butler B. J., Wrobel J. M., 2011, ApJ, 739, L1
Peterson J. R., Fabian A. C., 2006, Phys. Rep., 427, 1
Rafferty D. A., Bîrzan L., Nulsen P. E. J., McNamara B. R., Brandt W. N., Wise M. W., Röttgering H. J. A., 2013, MNRAS, 428, 58
Randall S. W. et al., 2011, ApJ, 726, 86
Rieke G. H., Alonso-Herrero A., Weiner B. J., Pérez-González P. G., Blaylock M., Donley J. L., Marcillac D., 2009, ApJ, 692, 556
Russell H. R., Sanders J. S., Fabian A. C., 2008, MNRAS, 390, 1207
Salomé P., Combes F., 2003, A&A, 412, 657
Salomé P. et al., 2006, A&A, 454, 437
Salomé P., Combes F., Revaz Y., Downes D., Edge A. C., Fabian A. C., 2011, A&A, 531, A85
Sanders J. S., 2006, MNRAS, 371, 829
Sanders J. S., Fabian A. C., 2002, MNRAS, 331, 273
Sanders J. S., Fabian A. C., 2006, MNRAS, 370, 63
Sanders J. S., Fabian A. C., 2007, MNRAS, 381, 1381
Sanders J. S., Fabian A. C., Dunn R. J. H., 2005, MNRAS, 360, 133
Sanders J. S., Fabian A. C., Taylor G. B., 2009, MNRAS, 396, 1449
Sanders J. S., Fabian A. C., Frank K. A., Peterson J. R., Russell H. R., 2010, MNRAS, 402, 127
Schlegel D. J., Finkbeiner D. P., Davis M., 1998, ApJ, 500, 525
Scodeggio M. et al., 2005, PASP, 117, 1284
Smith R. K., Brickhouse N. S., Liedahl D. A., Raymond J. C., 2001, ApJ, 556, L91
Sparks W. B., Macchetto F., Golombek D., 1989, ApJ, 345, 153
Sun M., 2009, ApJ, 704, 1586
Sun M., 2012, New Jo. Phys., 14, 045004
Sun M., Donahue M., Voit G. M., 2007, ApJ, 671, 190
Sun M., Voit G. M., Donahue M., Jones C., Forman W., Vikhlinin A., 2009, ApJ, 693, 1142
Wakker B. P., Schwarz U. J., 1988, A&A, 200, 312
Werner N. et al., 2010, MNRAS, 407, 2063
Werner N. et al., 2013, ApJ, 767, 153
Wilman R. J., Edge A. C., Swinbank A. M., 2006, MNRAS, 371, 93
Wilman R. J., Edge A. C., Swinbank A. M., 2009, MNRAS, 395, 1355
Zanichelli A. et al., 2005, PASP, 117, 1271

This paper has been typeset from a TEX/LATEX file prepared by the author.